*Global-scale assessment and inter-comparison
of recently developed/reprocessed microwave
satellite vegetation optical depth products*

Massachusetts Institute of Technology

Global-scale assessment and inter-comparison of recently developed/reprocessed microwave satellite vegetation optical depth products

Xiaojun Li [a], Jean-Pierre Wigneron [a,*], Frédéric Frappart [a,b], Lei Fan [c], Philippe Ciais [d], Rasmus Fensholt [e], Dara Entekhabi [f], Martin Brandt [e], Alexandra G. Konings [g], Xiangzhuo Liu [a], Mengjia Wang [a,h], Amen Al-Yaari [i], Christophe Moisy [a]

[a] INRAE, UMR1391 ISPA, Université de Bordeaux, F-33140, Villenave d'Ornon, France
[b] Laboratoire d'Etudes en Géophysique et Océanographie Spatiales (LEGOS), 31400 Toulouse, France
[c] School of Geographical Sciences, Nanjing University of Information Science and Technology, Nanjing 210044, China
[d] Laboratoire des Sciences du Climat et de l'Environnement, CEA/CNRS/UVSQ/Université Paris Saclay, Gif-sur-Yvette, France
[e] Department of Geosciences and Natural Resource Management, University of Copenhagen, Copenhagen, Denmark
[f] Massachusetts Institute of Technology, Department of Civil and Environmental Engineering, Cambridge, MA 02139, USA
[g] Department of Earth System Science, Stanford University, Stanford, CA 94304, USA
[h] State Key Laboratory of Remote Sensing Science, Faculty of Geographical Science, Beijing Normal University, Beijing 100875, China
[i] Sorbonne Université, UMR 7619 METIS, Case 105, 4 place Jussieu, Paris F-75005, France

ARTICLE INFO

ABSTRACT

The vegetation optical depth (VOD), a vegetation index retrieved from passive or active microwave remote sensing systems, is related to the intensity of microwave extinction effects within the vegetation canopy layer. This index is only marginally impacted by effects from atmosphere, clouds and sun illumination, and thus increasingly used for ecological applications at large scales. Newly released VOD products show different abilities in monitoring vegetation features, depending on the algorithm used and the satellite frequency. VOD is increasingly sensitive to the upper vegetation layer as the frequency increases (from L-, C- to X-band), offering different capacities to monitor seasonal changes of the leafy and/or woody vegetation components, vegetation water status and aboveground biomass. This study evaluated nine recently developed/reprocessed VOD products from the AMSR2, SMOS and SMAP space-borne instruments for monitoring structural vegetation features related to phenology, height and aboveground biomass.

For monitoring the seasonality of green vegetation (herbaceous and woody foliage), we found that X-VOD products, particularly from the LPDR-retrieval algorithm, outperformed the other VOD products in regions that are not densely vegetated, where they showed higher temporal correlation values with optical vegetation indices (VIs). However, LPDR X-VOD time series failed to detect changes in VOD after rainfall events whereas most other VOD products could do so, and overall daily variations are less pronounced in LPDR X-VOD. Results show that the reprocessed VODCA C- and X-VOD have almost comparable performance and VODCA C-VOD correlates better with VIs than other C-VOD products. Low frequency L-VOD, particularly the new version (V2) of SMOS-IC, show a higher temporal correlation with VIs, similar to C-VOD, in medium-densely vegetated biomes such as savannas (R ~ 0.70) than for other short vegetation types. Because the L-VOD indices are more sensitive to the non-green vegetation components (trunks and branches) than higher frequency products, they are well-correlated with aboveground biomass: (R ~ 0.91) across space between predicted and observed values for both SMOS-IC V2 and SMAP MT-DCA. However, when compared with forest canopy height, results at L-band are not systematically better than C- and X-VOD products. This revealed specific VOD retrieval issues for some ecosystems, e.g., boreal regions. It is expected that these findings can contribute to algorithm refinements, product enhancements and further developing the use of VOD for monitoring above-ground vegetation biomass, vegetation dynamics and phenology.

* Corresponding author.
   E-mail address: jean-pierre.wigneron@inrae.fr (J.-P. Wigneron).

1. Introduction

Microwave vegetation optical depth (VOD), as a promising ecological indicator, is directly proportional to the vegetation water content (VWC) of the aboveground canopy biomass (Brandt et al., 2018; Jackson and Schmugge, 1991; Mo et al., 1982; Wigneron et al., 2017). Different VOD indices (referred to as VODs in the following) derived from microwave observations at relatively "high" frequencies such as Ku- (18.7 GHz), X- (10.7 GHz) or C- (6.9 GHz) band have been used to monitor phenology (Jones et al., 2011), vegetation fractional cover (Guan et al., 2012), the impact of El Niño events on vegetation in Australia (Liu et al., 2007), isohydricity patterns (Konings and Gentine, 2017) and aboveground biomass (AGB) dynamics (Liu et al., 2015). In recent years, VOD at L-band (1.4 GHz) has been established as a useful indicator for estimating the dynamics in AGB in tropical forests. This was made possible because of the lower extinction of low frequency radiations within the canopy layer, making L-band arguably more efficient for monitoring biomass in dense vegetation canopies (Brandt et al., 2018; Fan et al., 2019; Tian et al., 2018; Wigneron et al., 2020). In comparison to optical-near infrared vegetation indices such as the Normalized Difference Vegetation Index (NDVI) and the Enhanced Vegetation Index (EVI), currently available VODs have a coarse spatial resolution, but are largely insensitive to effects from the atmosphere, clouds and sun illumination, in particular at low frequencies (L-, C- and X-bands).

Several VOD datasets used in the above-mentioned studies are derived from multiple spaceborne microwave sensors operating at different frequencies (Fernandez-Moran et al., 2017a; Li et al., 2020a; Liu et al., 2011). Among these sensors (satellites), the Advanced Microwave Scanning Radiometer 2 (AMSR2; Imaoka et al., 2012) is the successor of the Advanced Microwave Scanning Radiometer for EOS (AMSR-E; Koike et al., 2004), which enabled the fusion of the first long-term (1987–2008) global microwave-based VOD product (Liu et al., 2011). The ESA's Soil Moisture and Ocean Salinity (SMOS) and NASA's Soil Moisture Active Passive (SMAP) are two L-band sensors (Entekhabi et al., 2010; Kerr et al., 2010) which are designed for monitoring surface soil moisture (SM) in moderately and densely vegetated areas (Wigneron et al., 2017). While the main objective of these satellite missions was to monitor SM at global scale, the accurate retrieval of SM using radiative transfer models requires the consideration of the extinction effects of the vegetation layer, which are parameterized by the VOD index (Mo et al., 1982; Wigneron et al., 2007). In particular, the SMOS satellite has multi-angular capabilities, allowing simultaneous retrievals of SM and VOD (Wigneron et al., 2000), while multi-temporal VOD retrieval approaches have been developed for SMAP (Konings et al., 2016, 2017). Thus, both the SMOS and SMAP missions support the development of a separate VOD product in addition to the original SM product. Note that some specific satellite products focus only on SM, as the Japan Aerospace Exploration Agency (JAXA) standard SM products (Njoku et al., 2003). Recently, VOD products have been combined to long-term time series by blending multiple microwave sensors, such as the new global land parameter data record (LPDR) X-band VOD derived from AMSR-E and AMSR2 (Du et al., 2017b), and the global long-term microwave VOD Climate Archive (VODCA; Moesinger et al., 2020) produced by the Vienna University of Technology (TU Wien) including Ku-, X- and C-band VOD.

Assessing the performance of these remotely sensed VOD retrievals is crucial to improve their quality and evaluate their potential applications in many fields such as monitoring AGB, vegetation dynamics and phenology. However, VOD, like NDVI, is a radiometric variable rather than a well-defined and "easily validated" geophysical parameter (Liu et al., 2011). Evaluation based on field data of different vegetation components is rare (Brandt et al., 2019) and most evaluations of VOD datasets are based on a side-by-side comparison with proxies of the vegetation greenness based on optical vegetation indices (Du et al., 2017b; Grant et al., 2016; Jones et al., 2011; Karthikeyan et al., 2019; Lawrence et al., 2014; Li et al., 2020a; Liu et al., 2011; Moesinger et al.,

2020; Tian et al., 2016; Tong et al., 2019), including NDVI, EVI and Leaf Area Index (LAI). These previous comparisons revealed that VOD can generally capture vegetation seasonal cycles and interannual variations in a similar fashion as NDVI (Li et al., 2020a; Liu et al., 2011) and LAI (Moesinger et al., 2020; Cui et al., 2020). However, unlike NDVI, which is restricted to the upper green canopy layer, microwave-based VOD is able to sense the entire vegetation deeper within the canopy, with different layers and depths depending on the penetration capability of the observation frequency. Hence, NDVI saturates quickly as vegetation density increases and the green canopy closes, while VOD is sensitive to both the leaf and woody component of vegetation and not restricted to the upper canopy. Moreover, VOD is related to the water content of the vegetation canopy (i.e., VWC) that cannot be observed by optical indices. Lower frequencies (L-band) observations are sensitive to the water content present in the whole vegetation layer including the woody components of the vegetation, while higher frequencies (C- and X-band) observations are more sensitive to the water content of the upper layer of the vegetation canopy and, consequently, to the green vegetation components (leaves and stems for herbaceous vegetation, crown and leafy part of trees in forests). Therefore, evaluating VOD against optical indices should be limited to relatively low-density vegetation canopies. In particular, the optical indices are not a good reference for evaluating the capabilities of low frequency VODs (such as L-band VOD) for monitoring biomass, in particular over moderate to highly dense forests, especially in tropical regions.

As VWC is determined by the quantity of vegetation (parameterized by biomass) and the vegetation water status (parameterized by vegetation moisture content (M_g (kg/kg), the ratio between wet biomass and total (wet + dry) biomass, i.e., $M_g = VWC/(VWC + B_s)$, where B_s represents vegetation dry biomass)), VOD can thus provide information on AGB and the vegetation water status and stress of the vegetation canopy (Frappart et al., 2020; Togliatti et al., 2019). By assuming that the yearly average of M_g is relatively constant from year to year, which can be confirmed in intact forest regions and non-affected by severe drought/mortality events (Frappart et al., 2020), the yearly average of VOD can be considered as a good proxy of AGB (Liu et al., 2015; Brandt et al., 2018). Moreover, the function relating VOD to AGB has been established from a spatial calibration in several studies (see Frappart et al., 2020 for a review and more details on that topic). As the yearly averaged VOD computed at different frequencies is strongly correlated with the woody vegetation (Brandt et al., 2018; Brandt et al., 2019; Wigneron et al., 2017), the evaluation of VOD retrievals can be based on comparisons with AGB products. With the ongoing development of VOD retrieval algorithms/products at different frequencies, efforts have been made to compare the sensitivity of different VODs to forest carbon stocks. In the following, we will use L-VOD, C-VOD and X-VOD to denote the VOD products at L-, C- and X-bands, and so forth. Liu et al. (2015) computed a non-linear relationship between a reference map of AGB (Saatchi et al., 2011) and Ku/X/C-VOD products, and used this relationship to study the VOD-derived global biomass dynamics. Following this global analysis, Tian et al. (2016) confirmed the good relationship between AGB and Ku/C-VOD over the West African Sahel dryland ecosystems using temporal in-situ biomass measurements. Rodríguez-Fernández et al. (2018) conducted an inter-comparison of the spatial patterns of SMOS L-VOD products against four AGB benchmark maps over the African continent and revealed a high performance of the SMOS-INRA-CESBIO or SMOS-IC V105 L-VOD product relative to other SMOS products. More recently, Chaparro et al. (2019) compared the sensitivity of different VOD products at X-, C- and L-bands to AGB over tropical forests of Peru, southern Colombia and Panama.

However, very few studies have inter-compared VODs retrieved from different satellites and at different frequencies. For instance, inter-comparisons of VODs at L-band were limited to either the SMOS (Rodríguez-Fernández et al., 2018) or SMAP products (Chaparro et al., 2019), but to our knowledge the two products have rarely been inter-compared. Moreover, most inter-comparisons were conducted over

limited study areas for specific biomes or on a limited time scale. For example, Rodríguez-Fernández et al. (2018) and Chaparro et al. (2019) mostly focused on the yearly averaged VOD without considering the seasonal variations. For a better understanding of remotely sensed VODs and to facilitate improvements of the retrieval algorithms for future space-borne missions, the evaluation/inter-comparison of VOD products from different sensors and frequencies for a variety of spatio-temporal conditions is essential. Furthermore, new VOD algorithms and new versions of VOD products, such as the SMOS-IC version 2 (V2) L-VOD recently designed by INRAE Bordeaux (Li et al., 2020b; Wigneron et al., Submitted), are not yet comprehensively evaluated and inter-compared.

This study fills this gap by assessing and inter-comparing globally nine VOD products at three frequencies (X-, C- and L-bands; See Table 1). This evaluation considered the ability of VOD products to monitor both the seasonal vegetation cycle and the spatial distribution of AGB. Consequently, the objectives of this study are: (1) to assess and inter-compare the sensitivity of VODs (at L-, C- and X-bands) to AGB, as well as to compare those products with optical vegetation indices from Moderate Resolution Imaging Spectroradiometer (MODIS) considering both seasonal and annual spatial variations at the global scale; and (2) to examine the performance of the nine VODs in various biomes reflecting different environmental conditions. The second objective provides insight in how satellite-based VOD retrievals may be impacted by land cover features (vegetation structure, phenology, etc.) and heterogeneity.

2. Datasets

2.1. Remotely sensed VOD products

Table 1 presents an overview of the VOD datasets included in this study, mainly from SMOS, SMAP and AMSR2. More details about these satellite-based VOD products are provided in Appendix A.

To get an overview of the various approaches used in the VOD retrievals, we summarized the main differences in the algorithms used (Table 2). The brightness temperature (TB) measured by the passive microwave radiometers measures the natural microwave emission from the land surfaces. All these algorithms use a simple 0th-order Tau-Omega (τ-ω) radiative transfer model as the starting point to simulate the TB (Mo et al., 1982, Wigneron et al., 2017 for a review). As summarized in Table 2, the main differences in the VOD retrieval algorithms can be distributed in different categories, considering the parameterizations of the physical temperature including the effective soil and vegetation temperatures, surface roughness, effective scattering albedo, and dielectric mixing models. For example, unlike the other algorithms, where the roughness effects are estimated from a separate roughness correction step, the LPDR algorithm assumes a constant dry soil

emissivity to facilitate the VOD retrieval process, thus its VOD incorporate the soil roughness effects (Jones et al., 2010; Mladenova et al., 2014). VODCA is a fusion of VOD retrieval results from multiple sensors after co-calibration via cumulative distribution function matching using AMSR-E as the scaling reference (Moesinger et al., 2020). We did not list the VODCA retrieval algorithm separately as it is an updated version of LPRM V5, not yet available to the public. Readers are referred to Table 2 in Scanlon et al. (2020) for more details about this algorithm.

2.2. Evaluation datasets

2.2.1. MODIS vegetation indices

Two optical vegetation indices (VIs), NDVI and EVI, were compared with each VOD product. These two VIs were chosen as both are regarded as proxy for green vegetation cover (Weber et al., 2020). In particular, NDVI climatology is also used to estimate VOD in the inversion algorithm of the official NASA SMAP soil moisture products (Chan et al., 2013; Dong et al., 2018). Compared to NDVI, EVI is designed to decouple the canopy background signals and reduce atmospheric influences and it is designed to be less susceptible to saturation over forest areas (Huete et al., 2002). More information on NDVI and EVI are summarized in Table S1. In this study, the 16-day MODIS product (MOD13A2 Collection 6) was used to obtain the NDVI and EVI. Global MOD13A2 data is provided as a gridded level-3 product projected on the Sinusoidal projection with a spatial resolution of 1 km. To retain high-quality observations, we filtered out pixels not flagged as 'good quality' and pixels with snow/ice, cloud cover, and non-land as done by Grant et al. (2016). NDVI and EVI were subsequently aggregated to 25 km using nearest-neighbor interpolation.

2.2.2. Lidar tree height

The global tree height dataset from Simard et al. (2011) was used to assess the dependency of VOD on vegetation density. This height dataset was produced at 1 km resolution using lidar data collected in 2005 by the Geoscience Laser Altimeter System (GLAS) sensor. In addition, estimates over the areas not directly covered by the lidar footprint are made by combining relevant auxiliary data with Random Forest models. The lidar-derived data were chosen here not only because the total amount of vegetation is related to canopy height (Asner et al., 2012), but GLAS is also widely used as a primary source of information for carbon stock databases, reflecting the ability of tree height data for comparison purposes. Further details about this product and algorithm are described in Simard et al. (2011), and data can be freely downloaded at https://webmap.ornl.gov/ogc/dataset-.jsp?ds_id=10023. The dataset was aggregated (using linear averaging) to the VOD resolution (i.e. 25 km).

Table 1
Overview of the VOD datasets used in this study. Our study period is 04/2015–12/2017 as this period was sufficient to analyze seasonal variations in VOD.

Variable name	Dataset/Sensor	Frequency	Metadata Period	Sampling	Method/Algorithm	Reference
SMAP L-VOD	SMAP	1.4GHz	04/2015–09/2020	Daily, 9 km	MT-DCA	Konings et al. (2017)
IC V105 L-VOD	SMOS	1.4GHz	01/2010–09/2020	Daily, 25 km	SMOS-IC V105	Fernandez-Moran et al., 2017a
IC V2 L-VOD					SMOS-IC V2	Wigneron et al. (Submitted)
AMSRU X-VOD	AMSR-E and AMSR2	10.7GHz	01/2002–12/2019	Daily, 25 km	LPDR V2	Du et al. (2017a)
AMSR2 X-VOD	AMSR2	10.7GHz	07/2012–01/2020	Daily, 25 km	LPRM V5	Owe et al. (2008)
AMSR2 C1-VOD		6.9 GHz				
AMSR2 C2-VOD		7.3 GHz				
VODCA X-VOD	WindSat, AMSR-E, AMSR2 and TMI	10.65 GHz, 10.7 GHz	12/1997–12/2018	Daily, 0.25°	LPRM V6	Moesinger et al. (2020)
VODCA C-VOD	WindSat, AMSR-E and AMSR2	6.93 GHz, 7.3 GHz, 6.8GHz	06/2002–12/2018			

MT-DCA = multi-temporal dual-channel algorithm; LPRM = Land Parameter Retrieval Model.

Table 2

Summary of key differences among the SMOS-IC, MT-DCA, LPDR V2 and LPRM V5 retrieval algorithms.

Algorithm	SMOS-IC	MT-DCA	LPDR V2	LPRM V5
Observation	Multi-angular and dual polarization SMOS L3 T_B	Enhanced SMAP dual polarization T_B at a fixed incidence angle of 40°	Calibrated T_B retrieval records from both AMSR-E and AMSR2	AMSR2 spatial-resolution-matched T_B (L1SGRTBR)
Effective soil temperature	$T_G = f(T_{soil\_surf}, T_{soil\_depth})$ $T_{soil\_surf}, T_{soil\_depth}$ from Layer 1 & 3 of ECMWF $C_T = min\left(\left(\frac{SM}{w_o}\right)^{b_0}, 1\right), W_o =$ 0.3 m³/m³; $b_o = 0.3$	$T_G = f(T_{soil\_surf}, T_{soil\_depth})$ $T_{soil\_surf}, T_{soil\_depth}$ from Layer 1 & 2 of GEOS-5 $C_T = 0.246$	$T_G = f(T_{BP(18.7GHz)}, T_{BP(23.8GHz)})$ (P = H, V) using an iterative algorithm approach (Jones et al., 2010)	$T_G = LST = f(T_{Bv(37GHz)})$ LST derived from the method of Holmes et al. (2009)
Vegetation temperature	T_C = ECMWF skin temperature	$T_C = T_G$	$T_C = T_G$	$T_C = T_G$
Vegetation modelling	τ-ω model (Mo et al., 1982)	τ-ω model (Mo et al., 1982)	τ-ω model (Mo et al., 1982)	τ-ω model (Mo et al., 1982)
Soil roughness modelling	H-Q-N modelling (Wang and Choudhury, 1981) H_R values from Parrens et al. (2016) $N_{RP} = -1$ (P = H, V) over short vegetation $N_{RV} = -1, N_{RH} = 1$ over forests $Q_R = 0$	H-Q-N modelling (Wang and Choudhury, 1981) Assuming a constant roughness root-mean-square height of 0.13 (being the basis for formulations of H_R) $N_{RP} = 0$ (P = H, V) $Q_R = 0$	dry bare soil emmissivity $H_R = -, Q_R = -$	H-Q-N modelling (Wang and Choudhury, 1981) $N_{RP} = 1$ (P = H, V) $H_{R(10.7GHz)} = 0.18;$ $H_{R(7.3GHz)} = 0.09;$ $H_{R(6.9GHz)} = 0.09;$ $Q_{R(10.7GHz)} = 0.127;$ $Q_{R(7.3 GHz)} = 0.115;$ $Q_{R(6.9 GHz)} = 0.115;$
Effective scattering albedo	ω calibrated based on IGBP classifications	ω is retrieved simultaneously with SM and VOD	ω is prescribed as a constant value of 0.06	$\omega_{10.7GHz} = 0.06$ $\omega_{7.3GHz} = 0.05$ $\omega_{6.9GHz} = 0.05$
Dielectric mixing model	Mironov et al. (2004)	Mironov et al. (2004)	Dobson et al. (1985)	Wang and Schmugge (1980)

T_B = brightness temperature; T_G = effective soil temperature; T_C = vegetation canopy temperature; LST = land surface temperature; T_{soil_surf} = surface soil temperature; T_{soil_depth} = deep soil temperature; C_T = parameters (Choudhury effective temperature scheme); W_o, b_o = fitting parameters (Wigneron effective temperature scheme); ECMWF: European Centre for Medium-Range Weather Forecasts; GEOS-5: Goddard Earth Observing System Model, Version 5; H_R = roughness parameter; N_{RP} = roughness parameter accounting for polarization dependency; Q_R = polarization mixing coefficient; ω = effective scattering albedo; In LPDR, the Dobson dielectric model is only used for the retrieval of SM as the VOD retrieval considers a constant dry soil emissivity (Mladenova et al., 2014).
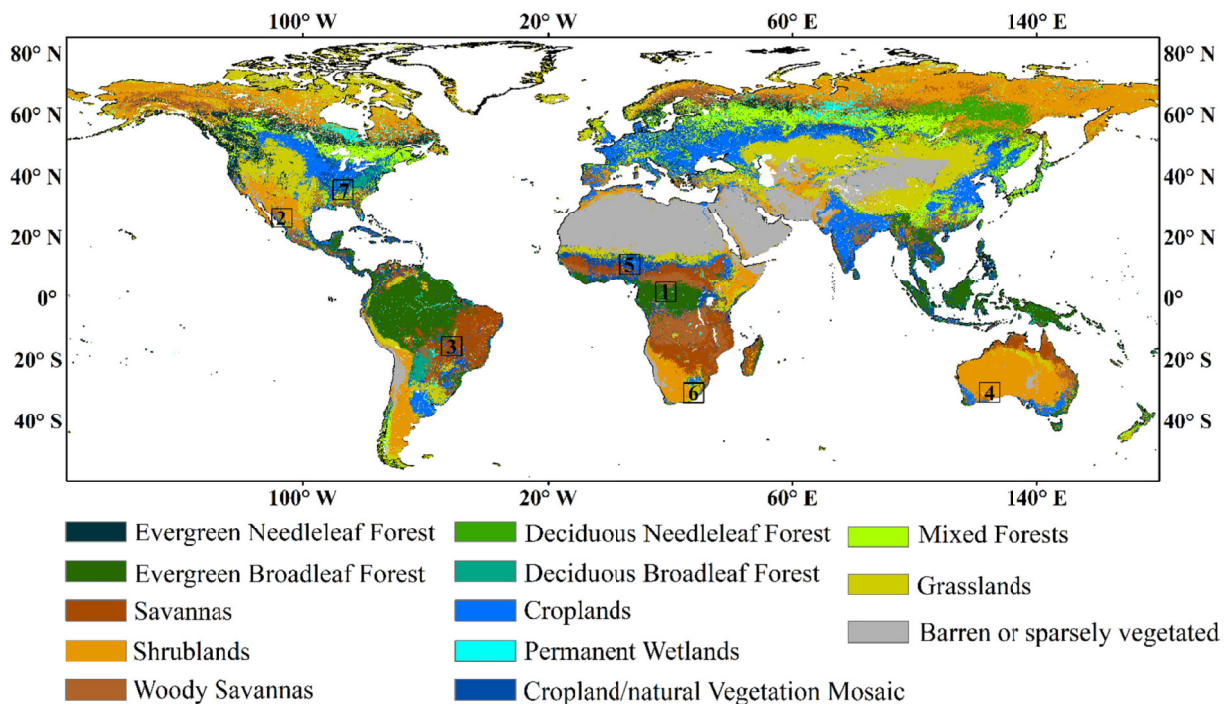
Fig. 1. Distribution of the IGBP land cover types. The boxes on the map indicate the selected sites (pixels) to illustrate the main features of the nine VOD products for a variety of vegetation conditions.

2.2.3. Aboveground biomass

We compared VOD with AGB provided by the global map updated from Saatchi et al. (2011) (Saatchi et al., unpublished results) to assess the relationships of different VOD products to the spatial variations in aboveground vegetation carbon stocks. The 1-km resolution Saatchi AGB map is produced from a variety of datasets (e.g., in-situ inventory plots, MODIS and Quick Scatterometer (QuikSCAT) products). The detailed methodology for generating this dataset is described in Saatchi et al. (2011). The map obtained in this study (referred as to Saatchi AGB) represents AGB circa 2015 (Carreiras et al., 2017). We selected this dataset as an AGB benchmark map because it has been widely used as a reference map to obtain calibration coefficients for converting L-VOD to carbon density (Tong et al., 2019; Fan et al., 2019; Wigneron et al., 2020). In these studies, best correlation scores between VOD and AGB were generally obtained using Saatchi AGB, confirming the accuracy of the Saatchi et al. (2011) datasets. In our study, the static Saatchi AGB dataset was aggregated (using averaging) to 25 km scale to match the spatial resolution of the other datasets.

2.2.4. Ancillary datasets

Several additional datasets resampled to 25 km were also used to interpret the results. The MODIS-based global land cover climatology map (Fig. 1) was applied to analyze the VOD inter-comparison results as a function of land cover types. This land cover map is generated by combining the 0.5 km MODIS product (MCD12Q1) in the International Geosphere-Biosphere Programme (IGBP) scheme, as described in Broxton et al. (2014). In addition, daily precipitation from NASA's Global Precipitation Measurement (GPM) IMERG Late Precipitation L3 1 day $0.1° \times 0.1°$ (version 06) was used to identify the influence of precipitation events on the temporal dynamics of VOD (Liu et al., 2011).

3. Methodology

3.1. VOD dataset pre-processing

The accuracy of the retrieved VOD data is generally highly variable depending on topography, presence of frozen land surface conditions (e. g., ice, snow), radio frequency interference (RFI), and pixel heterogeneity (e.g., water or urban fractions) (Fernandez-Moran et al., 2017a). Filtering out potentially spurious observations was an important step for the reliability of this study. Hence, the following data pre-processing strategies were applied: i) to guarantee a fair inter-comparison, the assessment of the VOD products was conducted for the same dates for all products, which covers the period from April 2015 to December 2017. This time period of about 2 years and a half was sufficient to analyze seasonal variations in VOD; ii) the assessment was performed only over pixels considering statistical error indicators (for example, the *p*-value to estimate the robustness of the information provided by correlation coefficients), which will be introduced in the following Section 3.2; iii) applying the following data filtering for all VOD retrievals:

- RFI. Microwaves emitted by artificial devices on the Earth's surface distort signals received by satellite sensors, resulting in unreliable VOD retrievals. RFI intensity varies with frequency and location and its impact varies with the sensor. For instance, at L-band, the SMAP sensor, which is more recent than SMOS, is equipped with improved RFI filtering techniques; SMOS is more affected by RFI in Asia and Europe than elsewhere (Al-Yaari et al., 2019). Daily observations affected by RFI are partly filtered out in this study by using corresponding flags in each dataset as recommended by the data producers.
- Frozen soil. Due to the differences in the dielectric properties of water and ice, VOD retrievals are generally unreliable when the ground is frozen (Moesinger et al., 2020). Hence, we removed observations where the surface temperature was below 273.15 K. This was done with the available flags for those VOD datasets, e.g., SMOS-

IC provides a flag corresponding to frozen conditions (Fernandez-Moran et al., 2017a).
- Other potentially uncertain observations. In this study, we directly used land classification data to eliminate static water bodies. We also masked all pixels being "heterogeneous" or with a strong topography. Heterogeneity was determined when the summed fraction of urban, wetland, open water, and ice was greater than 10% (Fernandez-Moran et al., 2017a). Finally, negative VOD values, which are physically impossible, were removed.

The above filtering rules were applied independently to all daily-scale VOD retrievals. We then adopted bilinear interpolation to resample SMAP MT-DCA, AMSR2 and VODCA VOD to the same projection with a spatial resolution of 25 km. The same method has been utilized in other studies involving VOD processing (Brandt et al., 2018; Chaparro et al., 2019; Fan et al., 2019; Liu et al., 2018). Finally, the resulting daily VOD data were averaged per pixel to 16-day mean values to match the temporal resolution of the optical vegetation indices.

3.2. Methods for inter-comparison

A direct validation of the VODs at the global scale is not possible as there is a lack of consensus on the reference values from in-situ measurements or models to use (Li et al., 2020a). Several studies have shown that at the global scale, VOD values not only have a high spatio-temporal consistency with optical vegetation indices (Du et al., 2017b; Lawrence et al., 2014), but also have a fairly consistent spatial distribution with vegetation biomass and forest canopy height (Liu et al., 2011; Tian et al., 2016). Hence, comparing VOD values with related variables and proxies is an alternative method to evaluate the VOD performance which has often been used (Fernandez-Moran et al., 2017a; Li et al., 2020a; Rodríguez-Fernández et al., 2018). In this study, the temporal and spatial correlation between different VOD products and evaluation (vegetation-related) datasets were assessed using the Pearson correlation coefficient (R) (Grant et al., 2016; Lawrence et al., 2014; Li et al., 2020a). We also considered the probability value (p) as a measure of statistical significance; a level of $p < 0.05$ was used here.

To evaluate the ability of VOD to monitor AGB, we directly compared the spatial correlation between VOD and aboveground carbon density. We used a logistic function to fit the relationship between VOD and AGB following the method used by Rodríguez-Fernández et al. (2018):

$$AGB = \frac{a}{1 + e^{-b(VOD-c)}} + d \qquad (1)$$

where AGB and VOD represent aboveground carbon density and vegetation optical depth at each frequency, respectively, and *a*, *b*, *c* and *d* are best-fit parameters. The fitted curve gives AGB (Mg ha^{-1}) as a function of VOD (dimensionless). Thus, the units of *a* and *d* are Mg ha^{-1}, while *b* and *c* are dimensionless quantities. Spatial correlation computed between predicted (using the AGB – VOD fit given in Eq. (1)) and observed AGB is also presented to evaluate the accuracy of the AGB predictions based on different VOD products.

In addition to the above metrics, we adopted the Hovmöller diagram to compare the spatio-temporal patterns of VOD for the nine products. This diagram is a two-dimensional plot that shows the time–latitude variations of a longitudinally averaged variable (Hovmöller, 1949), highlighting consistency and differences between the nine VOD products. Moreover, an analysis at the pixel-scale was conducted to compare the nine VOD datasets for a variety of biomes: seven pixels taking into consideration relatively homogeneous land cover conditions (measured using the Gini–Simpson index; Simpson, 1949) and contrasting vegetation types (see Fig. 1 and Table 3) were selected to compare the VOD time series from different products. Although this comparison was limited to seven locations that cannot cover the full range of climatic, vegetation, and soil conditions at a global scale, the comparison at the pixel-scale allowed us to analyze and illustrate some of the main

Table 3
Location and type of biome of the seven sites (pixels) selected to compare the different VOD time series.

	Location	Latitude	Longitude	Land Cover
1	Congo	2.060° N	18.545° E	Evergreen broadleaf forest
2	Mexico	25.641° N	106.988° W	Mixed forests
3	Brazil	15.993° S	51.484° W	Savannas
4	South Australia	30.747° S	124.106° E	Open shrublands
5	Nigeria	11.551° N	7.133° E	Croplands
6	South Africa	31.432° S	27.882° E	Grasslands
7	South East US	35.173° N	86.758° W	Cropland/natural vegetation mosaic

characteristics of the nine VOD datasets (Al-Yaari et al., 2014; Karthikeyan et al., 2019).

All the above defined statistical indicators were only calculated on common pixels that contained observations for all nine VOD products. For example, to obtain the spatial R values between VOD and the evaluation datasets, we used the time averaged values computed only when each of the nine 16-day mean VOD data were available from the different datasets. However, in a second step, to ensure a good overview of all datasets in the analysis of the spatial patterns and of the Hovmöller diagram, all available data has been kept for the different VOD products.

4. Results

4.1. Spatial patterns and temporal dynamics at global scale

At a global scale, all VODs show a similar spatial pattern, matching

MODIS LAI and canopy height, with highest VOD values in tropical (e.g., Amazon and Congo basins) and boreal (e.g., Canada, Northern Russia) forests and low VOD values in sparsely vegetated and dry areas (e.g., Sahara in northern Africa, desert areas in Australia and central Asia) (Fig. 2a-l). The same patterns can be found in the AGB map (Fig. 2o). There are a few exceptions and notably the AGB values are much higher in the tropical and eastern Russia forests than in western Russia, Canada and Alaska forests, while VOD is about equally high in each of these areas. In terms of absolute VOD values, it can be seen that there are large differences even for a given frequency. For instance, considering X-band, LPDR V2 VOD is obviously larger than LPRM V5 and VODCA VOD (by a factor of about 2 in some densely vegetated regions). Considering C-band, the harmonized VODCA C-VOD value is generally lower than the value of LPRM V5 C1- and C2-VOD, while the latter two are very similar. As for L-VOD, both versions of SMOS-IC have lower values than SMAP MT-DCA, especially in eastern Brazil, southern China, and boreal forests. According to the theoretical principle that propagation of the microwave radiations decreases with frequency due to increasing extinction effects, the VOD values in the high frequency band should theoretically be larger than those in the lower frequency bands (Moesinger et al., 2020). However, the VOD values obtained from the LPRM algorithm do not seem to support this theory; in particular, over southern Mexico, Amazon and Congo basins LPRM V5 X-VOD has lower values than LPRM V5 C-VOD (Fig. 2a, e–f). A deeper analysis of this signature is discussed in Section 5.1. Zonal VOD averages (side plots of Fig. 2) confirm the results presented above. It can be seen that the zonal averaged distribution of X-, C-, L-VOD and AGB is similar, that is, two obvious high VOD and AGB peaks can be noted around latitudes of ~0°N and ~ 60°N corresponding to regions of dense tropical and boreal forests. The sharp peak presented by L-VOD for the SMOS and SMAP products correspond better to the AGB peaks (Fig. 2p) as compared to the X- and C-VOD products which show more gentle and flat peaks (Fig. 2d and h). These
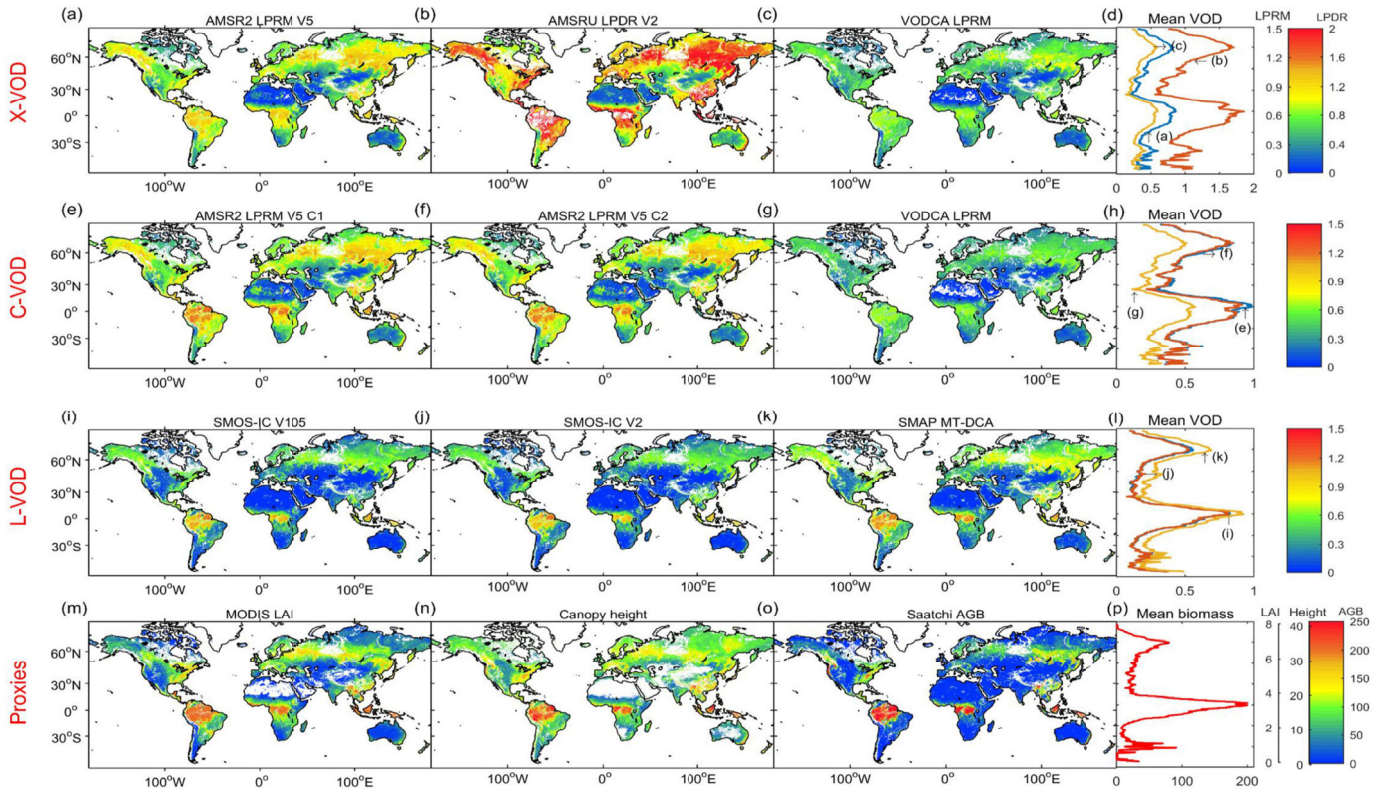
Fig. 2. Time averaged global maps of VOD from April 2015 to December 2017 for a) AMSR2 LPRM V5 X-VOD, b) AMSRU LPDR V2 X-VOD, c) VODCA LPRM X-VOD, e) AMSR2 LPRM V5 C1-VOD, f) AMSR2 LPRM V5 C2-VOD, g) VODCA LPRM C-VOD, i) SMOS-IC V105 L-VOD, j) SMOS-IC V2 L-VOD, k) SMAP MT-DCA L-VOD and of m) MODIS LAI (m²/m²), n) lidar vegetation height (m) and o) Saatchi AGB (Mg ha⁻¹). Side plots show zonal averages for d) X-VOD, h) C-VOD, l) L-VOD and p) biomass. Note: to ensure a good overview of all datasets after quality control, no inter-mask is applied here.

results are in line with the fact L-VOD is more sensitive to the whole biomass, including stems, while higher frequency VODs are more sensitive to the top of canopy and to leaf biomass, as found over Africa (Brandt et al., 2018).

Boxplots of the average VOD values per land cover class show that grasslands and shrublands as well as croplands have the lowest VOD values, followed by savannas (Fig. 3). In contrast, forests and biomes with more woody vegetation such as deciduous broadleaf, deciduous needleleaf, and mixed forests show higher VOD values, which is consistent with previous findings using in-situ biomass data and AMSR-E VODs over Sahel drylands (Tian et al., 2016). All VODs consistently show that evergreen broadleaf forest, mainly distributed in the wet tropics, has the highest VOD values. Interestingly, VODs from different algorithms/products were found to have a wide range of quantile values over shrublands and grasslands, but a narrow range over croplands despite the fact that planting density, crop types, and growing season vary across regions, and despite the fact that biomass and hydraulic behavior varies depending on crop types (Konings et al., 2017). As noted before, for a given IGBP class, the VOD values should theoretically increase with frequency. However, even if we exclude the reprocessed VODCA VOD and only compare the VODs obtained from the same algorithm and for the same mission, this theory is not fully supported. For example, for evergreen broadleaf forest, the median X-VOD value (~0.93) obtained from AMSR2 LPRM V5 is lower than the values of C1-VOD and C2-VOD (both ~1.05). There are also variations for observations in the same frequency range: at L-band, VOD values derived from SMAP MT-DCA are higher than those derived from both versions of

SMOS-IC for all IGBP categories. As observed from the spatial patterns shown in Fig. 2, the average VOD values of the two versions of SMOS-IC are very similar. It can also be seen that L-VOD values generally follow the decreasing trend in the AGB values from left to right in the plot, which is not clear in other VOD products.

VOD varies temporally and spatially, and this variability depends mainly on the season and latitude (Tian et al., 2018). We also evaluated the ability of all VODs to detect the spatio-temporal variations in the vegetation cycle, e.g., growth and senescence (Fig. 4). All nine VODs have some common periodical features. For instance, similarly to NDVI, a distinct seasonal pattern for all products can be seen in the Northern Hemisphere ($> 35°N$) with higher VOD values during the summer months corresponding to the period of maximum vegetation growth and leaf production (as expected). However, the amplitude (maximum − minimum) of the VODs in response to seasonal changes in vegetation structure and production differs. Specifically, the order of this amplitude is X-VOD > C-VOD > L-VOD. In the high latitudes of the Northern Hemisphere (between 45°N and 60°N), all X-VODs show a clear seasonality comparable to that of NDVI, followed by all C-VODs while all L-VODs present weaker seasonal dynamics. This can be related to the fact that VOD contains more information on the non-green woody component (e.g. woody stems and branches which are vegetation components with less seasonal changes than leaves) with decreasing frequency (Grant et al., 2016; Tian et al., 2016). So, even during leaf development in deciduous forests, L-VOD values are almost insensitive to leaf density, in agreement with tower-based experiments (Guglielmetti et al., 2007). This phenomenon is even more pronounced in tropical regions, where
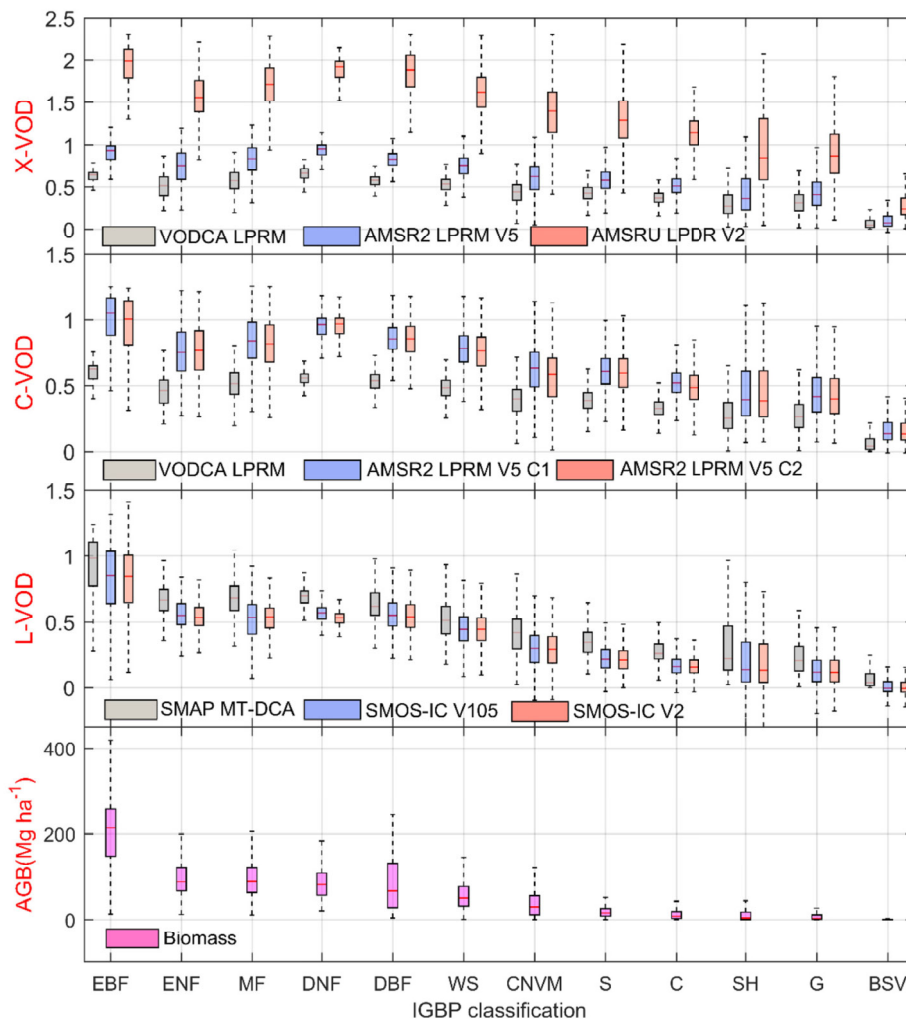
Fig. 3. Boxplots of VOD at three frequencies (X-, C- and L-band) and of biomass for different IGBP land cover classes. The vegetation IGBP classes are sorted by decreasing median values of the AGB values. The central mark within each box shows the median value, and the bottom and top edges mark the extent of the 25th and 75th percentiles. Whiskers include 99.3% of all data. EBF = evergreen broadleaf forest, ENF = evergreen needleleaf forest, MF = mixed forests, DNF = deciduous needleleaf forest, DBF = deciduous broadleaf forest, WS = woody savannas, CNVM = cropland/natural vegetation mosaic, S = savannas, C = croplands, SH = shrublands, G = grasslands, BSV = barren or sparsely vegetated.
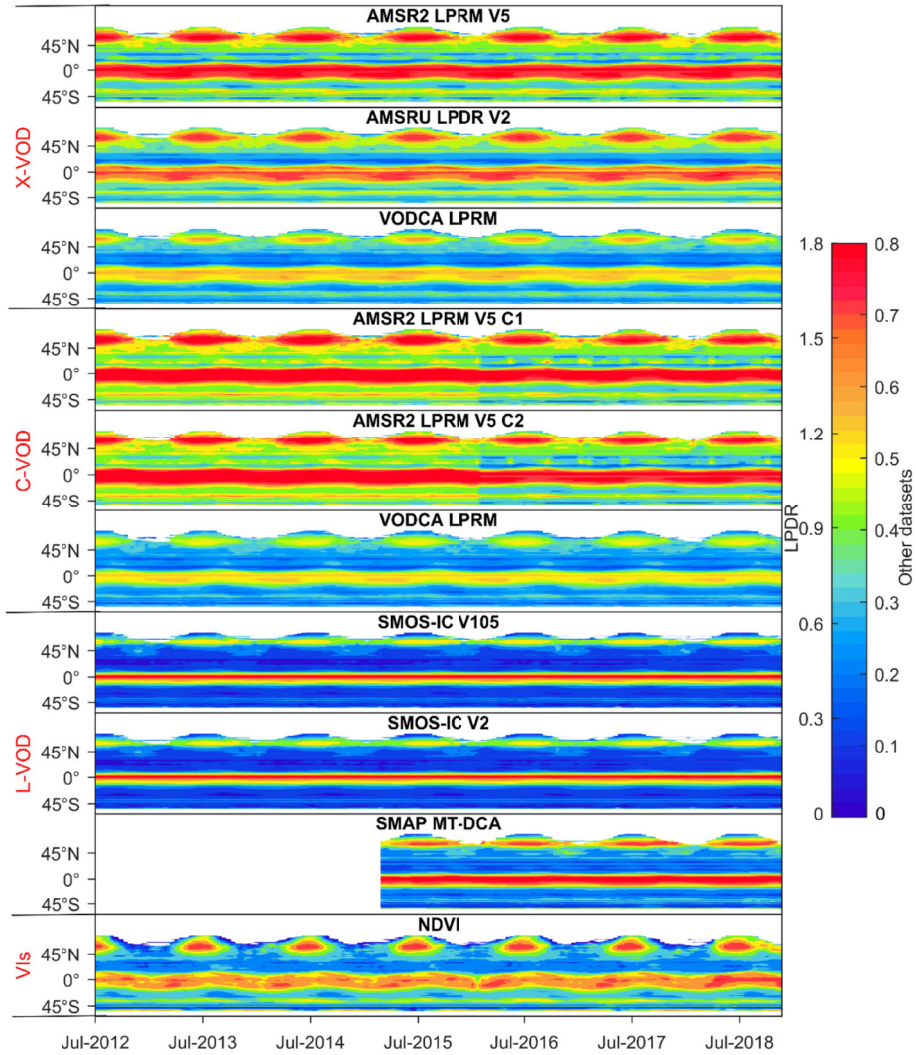
Fig. 4. Hovmöller diagrams showing the 16-day mean values per latitude for the nine VOD products at X-, C- and L-bands and for NDVI. Note that frozen soil conditions were removed during the data pre-processing (Section 3.1), so that there is no-data at higher latitudes in winter.

all L-VODs are almost constant. Surprisingly, since June 2015, the C1-VOD and C2-VOD values obtained by AMSR2 LPRM V5 are globally systematically lower than before and we did not find related literature to point out the specific reason for this discontinuity, nor if there a reason to think the raw AMSR2 observations changed in that time period.

4.2. Evaluating VOD against MODIS NDVI & EVI

4.2.1. Spatial correlation

The spatial correlation (R) of the nine VODs with mean NDVI and EVI is presented in Table 4, while the corresponding density plots are shown in Fig. 5 and Fig. S3 (with EVI). When considering the IGBP vegetation types altogether, all VODs were found to have a slightly higher correlation with NDVI (Bold items in Table 4; R=0.79–0.89) than with EVI (R=0.73–0.84). This could be related to the fact EVI is more sensitive to

Table 4
Spatial correlation between the nine VOD products at X-, C- and L-bands and NDVI/EVI for different short vegetation IGBP types.

Frequency	Product	NDVI							EVI						
		SH	WS	S	G	C	CNVM	R_total	SH	WS	S	G	C	CNVM	R_total
X-VOD	AMSR2 LPRM V5	0.81	0.38	0.72	0.72	0.60	0.73	**0.87**	0.77	0.23	0.71	0.64	0.53	0.65	**0.80**
	AMSRU LPDR V2	0.83	0.43	0.75	0.74	0.62	0.74	**0.89**	0.78	0.41	0.76	0.65	0.59	0.74	**0.84**
	VODCA LPRM	0.79	0.34	0.69	0.71	0.57	0.70	**0.86**	0.75	0.27	0.69	0.63	0.51	0.63	**0.79**
C-VOD	AMSR2 LPRM V5 C1	0.81	0.36	0.68	0.73	0.59	0.71	**0.87**	0.77	0.26	0.68	0.64	0.53	0.65	**0.80**
	AMSR2 LPRM V5 C2	0.82	0.33	0.63	0.71	0.48	0.65	**0.84**	0.78	0.15	0.62	0.63	0.49	0.56	**0.76**
	VODCA LPRM C	0.79	0.30	0.56	0.70	0.58	0.71	**0.86**	0.76	0.27	0.57	0.62	0.52	0.63	**0.80**
L-VOD	SMOS-IC V105	0.78	0.42	0.68	0.55	0.47	0.72	**0.79**	0.73	0.23	0.67	0.46	0.43	0.70	**0.73**
	SMOS-IC V2	0.78	0.41	0.69	0.57	0.48	0.72	**0.80**	0.74	0.27	0.68	0.48	0.44	0.71	**0.75**
	SMAP MT-DCA	0.77	0.33	0.64	0.52	0.44	0.69	**0.80**	0.74	0.18	0.65	0.44	0.41	0.69	**0.75**

Note: all the correlation coefficients are significant considering the criteria $p < 0.05$.
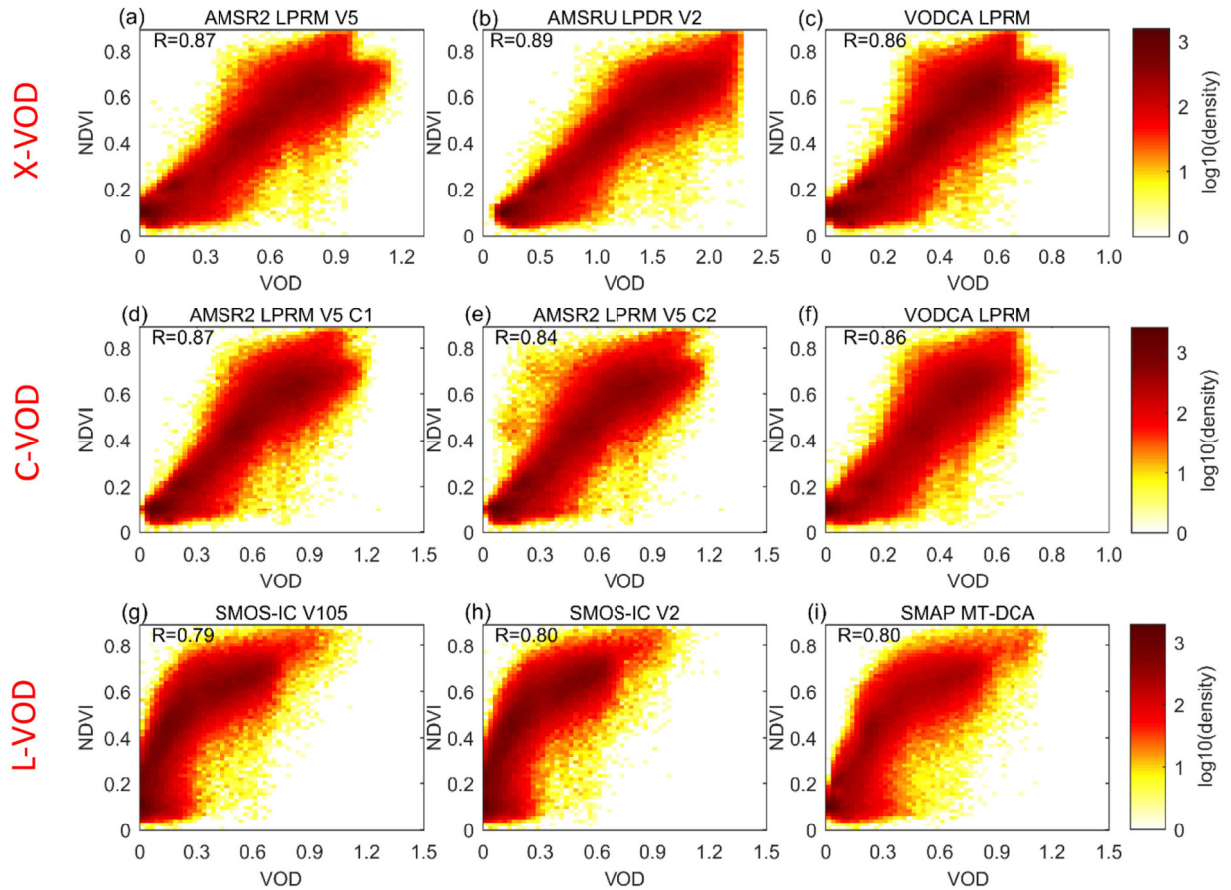
Fig. 5. Density scatter plots showing the spatial relationship between time averaged VOD values for the nine products at X-, C- and L-bands and NDVI at the global scale.

forest cover than to AGB as suggested by Chaparro et al., 2019. The highest correlation values were obtained between LPDR V2 X-VOD and NDVI/EVI, while SMOS-IC V105 L-VOD had the lowest correlation with NDVI/EVI, although its value is very close to the other L-VODs. We found that the slope between VOD and NDVI varies with VODs. The correlation between VOD and NDVI or EVI is found to be generally higher for higher frequencies (L-VOD < C-VOD < X-VOD), which is related to the fact that high-frequency VOD is sensitive to green vegetation which is not the case for low frequency VOD (Jones et al., 2013). Moreover, both NDVI and EVI saturate at moderate L-VOD values (~ 0.5) (Fig. 5 and Fig. S3). Therefore, as we mentioned in the introduction, only comparing with optical vegetation indices is not enough to evaluate low frequency VODs (such as L-VOD) that are relatively insensitive to green vegetation and more sensitive to non-green vegetation components.

Note that optical indices (i.e., NDVI or EVI) saturate when the vegetation cover is dense, so their applicability for a proper evaluation is limited to high frequency VOD. For a complementary comparison of VODs considering separately sparse and dense forest areas (i.e., evaluating VOD against forest canopy height), we refer to the supplementary material.

As the optical vegetation indices saturate over densely vegetated areas (Fig. 5) we listed only the spatial correlation between VODs and optical indices for relatively short vegetation IGBP types (i.e., non-forest and non-bare land types) in Table 4. The highest spatial correlation between VOD and vegetation indices can generally be found within shrublands, while the lowest correlation is for woody savannas followed by croplands, regardless of frequency or product (or algorithm). For X-VOD, the same R value ranking (AMSRU LPDR V2 > AMSR2 LPRM V5 > VODCA LPRM) was found over all short vegetation IGBP land cover

types, except for woody savannas where VODCA LPRM has a higher correlation value than AMSR2 LPRM V5 compared to EVI. AMSR2 C1-band (6.9 GHz) VOD is generally found to have higher (or comparable) correlations with optical indices than the C2-band (7.3 GHz) VOD for these IGBP vegetation types. Considering low frequency L-VOD, SMOS-IC V2 has higher or comparable spatial correlation values with NDVI or EVI for all vegetation types than V105 and SMAP MT-DCA. The spatial correlation (R) values between the three L-VODs and NDVI (or EVI) were found to be lower than those of C-VOD and X-VOD over grasslands and croplands, while the R values are comparable over the other IGBP types. SMOS-IC V2 L-VOD presents even higher correlation values than C-band VODs for savannas, woody savannas and cropland/natural vegetation mosaic.

4.2.2. Temporal correlation

We found that the spatial patterns of the temporal correlation (R) values between VODs and NDVI or EVI are generally similar for all VOD products, whether they are obtained at the same frequency or not (Fig. 6 and Fig. S4). LPDR V2 X-VOD presents the highest temporal R values with NDVI or EVI among the nine VOD products over most of the globe, especially in central and eastern Russia ($R > 0.75$, Fig. 6) where most other products show relatively low correlations. More generally, all X-VODs are better correlated with NDVI than C- and L-VODs over most regions of the globe, in particular in areas where annual rainfall controls vegetation production, e.g., over Australia, southern Africa, Sahel, eastern Brazil, Mexico, and also in eastern Canada, and eastern Russia. All VODs were found to have non-significant R values ($p > 0.05$) over desert areas in central Asia and northern Africa and in most tropical areas (e.g., Congo and Amazon basins) with a low inter-annual green vegetation dynamic. The temporal R values between VOD and NDVI (or
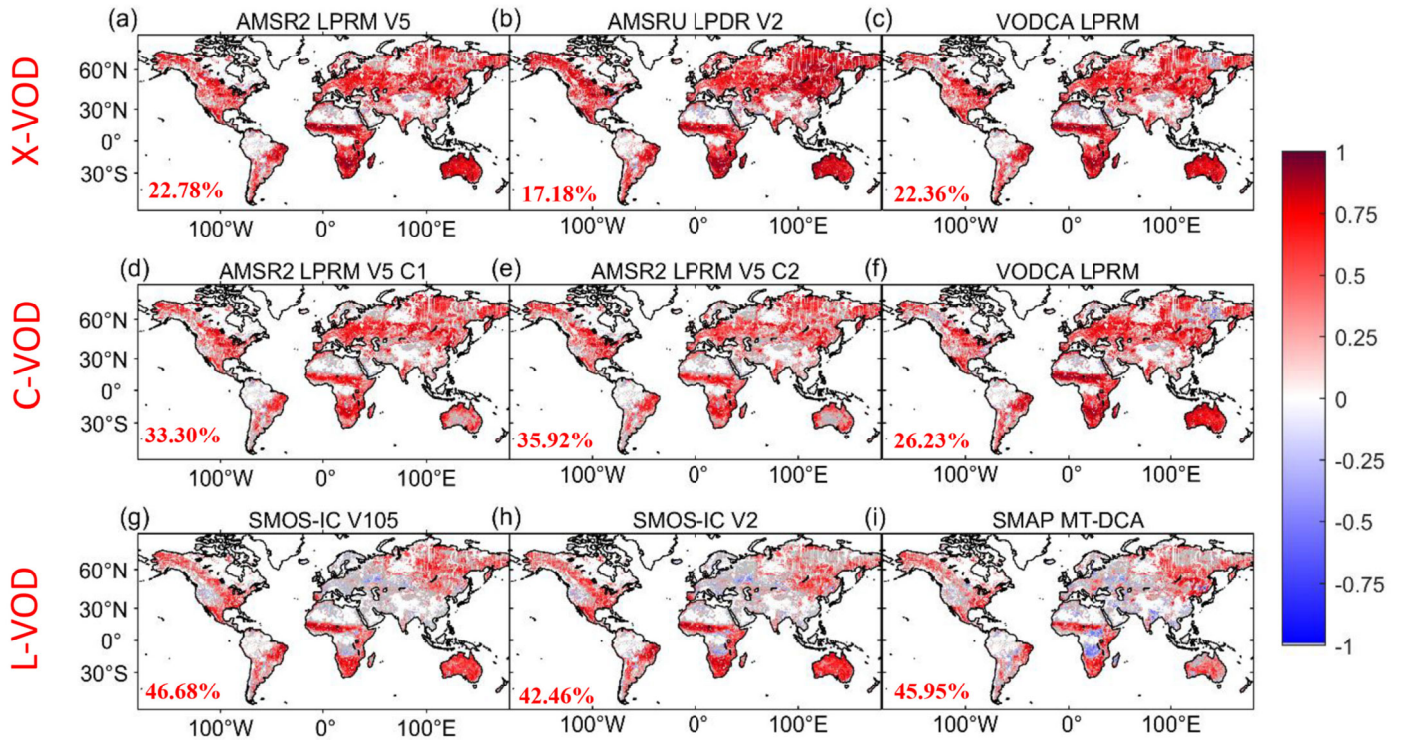
Fig. 6. Per-pixel temporal correlation (R) for the relationship between 16-day average values of the nine VODs at X-, C- and L-bands and MODIS NDVI from April 2015 to December 2017. Grey areas correspond to pixels where correlation is not significant ($p > 0.05$; their percentages are also given in the figure). White areas denote "no valid data".

EVI) increase with frequency (L-VOD < C-VOD < X-VOD) over most regions of the globe, e.g., eastern Canada, Russia, India, central and eastern Europe; another fact is that the proportion of pixels with non-significant correlation values is also decreasing. However, there are

some exceptions. For instance, reprocessed VODCA C- and X-VOD have almost comparable performance and both versions of SMOS-IC L-VOD still have higher temporal R values than AMSR2 LPRM V5 C1- and C2-VOD over eastern Brazil, western Sahel, south Africa and Australia.
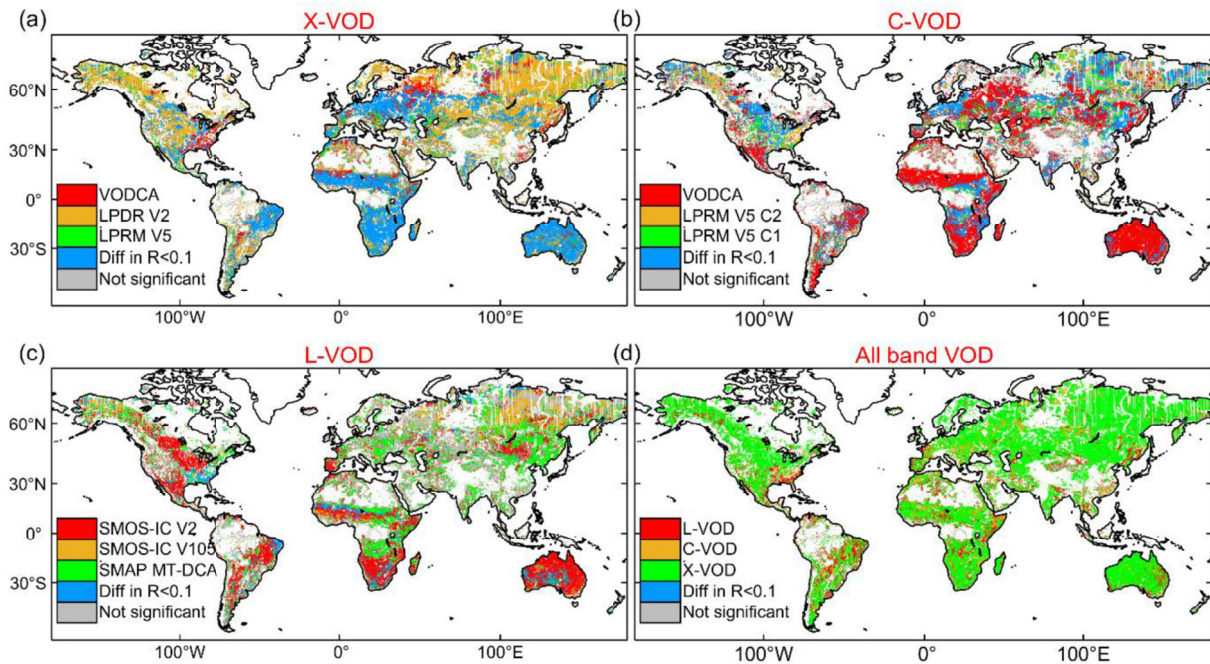
Fig. 7. Maps of VOD products showing the strongest correlation (R) values with MODIS NDVI for a) X-VOD; b) C-VOD; c) L-VOD; d) All-band VOD for each pixel. The pixels for which the difference in R is lower than 0.1 in absolute terms are indicated by a blue colour. Grey areas correspond to pixels where the correlation is not significant ($p > 0.05$). White areas denote "no valid data". (For interpretation of the references to colour in this figure legend, the reader is referred to the web version of this article.)

Interestingly, all L-VODs show a negative temporal correlation with NDVI or EVI (Fig. 6 and Fig. S4) in the dry tropical woodlands around the rain forests in the Congo Basin, in line with previous findings of the decoupling between seasonal changes in L-VOD (stem water content) and leaf phenology estimated from LAI (Tian et al., 2018, regions (i) and (ii) in their Fig. 3).

To get an easier overview of the comparison considering the observation frequency, a map showing which VOD product has the strongest per-pixel correlation with NDVI (and by a difference in correlation R of 0.1 at least in absolute terms) is provided for each frequency separately in Fig. 7 (and in Fig. S5 for EVI). Note that the relationship to NDVI can be negative especially for L-VOD in dry tropical woodlands, as discussed above (Fig. 6g-i). At X-band, the strongest correlations are generally found for AMSRU LPDR V2 (over 36.24% of the pixels without considering non-significant relationships), while VODCA VOD shows highest R values over the eastern US and western Russia, and has a comparable performance with AMSR2 LPRM V5 X-VOD for other regions (Fig. 6). At C-band, VODCA C-VOD presents the highest correlation values over 53.92% of the pixels (Fig. 7b); in the eastern US AMSR2 LPRM V5 C2 generally shows the highest correlation values. For L-VOD, SMOS-IC V2 shows generally the highest correlation values (42.44% of the pixels), except in some Northern Siberian regions, eastern Sahel, Kenya and Miombo woodlands in Tanzania, where stronger correlation values are obtained with SMAP MT-DCA (32.44% of the pixels). It is worth to note that the temporal correlation between SMOS-IC V2 and NDVI is generally better than that obtained using V105 in most regions of the globe, especially over Mexico, eastern Brazil, southern Africa and Australia (Fig. 6 and Fig. 7). When considering frequencies rather than products (Fig. 7d), it is also interesting to note that, although X-VOD presents stronger correlation values with NDVI over most of the globe, L-VOD correlates better with NDVI than X-VOD in some regions (e.g., eastern US, mid-west Brazil and Miombo woodlands (Fig. S5)). This may be caused by the different time lags between NDVI and VOD at different frequencies. So, more generally, a higher correlation value between NDVI and VOD cannot be directly interpreted as the ability of the VOD product to better capture the seasonal changes of vegetation. More details about the effects of time lags are discussed in 5.2. Similar plots using MODIS EVI confirm the results presented above for NDVI (Fig. S5) and, as for spatial correlation, lower temporal correlation values were obtained for the VOD/EVI relationship as compared to the VOD/NDVI relationship over most of the globe except in some eastern Europe and Northern Siberian regions (Fig. S6).

The highest temporal correlation with NDVI or EVI per IGBP vegetation type (Table S4) is found for savannas regardless of frequency or product; this case is illustrated by the time series of VOD and NDVI at the savannas site (Fig. 8c). In general, the VODCA C-VOD has temporal correlation values comparable (or relatively closer than the other C-VODs) to X-VOD for the listed vegetation types (Table 4). Excluding this reprocessed product, the temporal correlations between L- and C- VODs and NDVI (or EVI) were found to be lower than those obtained with X-VOD for these short vegetation types (including considering the IGBP types altogether), while both versions of SMOS-IC L-VOD and C-VOD have comparable correlations over most IGBP types except woody savannas and croplands. Among the three L-band VOD products, SMAP MT-DCA L-VOD shows relatively low temporal correlations with NDVI and EVI for these short vegetation types, which is reflected in Fig. 8 where the SMAP L-VOD time series remain relatively stable, even when NDVI has strong dynamics. A deeper analysis of this is discussed in Section 5.1. SMOS-IC (V2) shows higher temporal correlations than C-band VODs (e.g., AMSR2 LPRM V5 C1- and C2-VOD) for shrublands and savannas (Table S4), which is surprising. This may be due to the fact that L- and C-bands can both penetrate the canopy of medium-densely vegetated biomes well.

4.2.3. VOD time series

An analysis of the seasonal dynamics in the different VODs is here conducted based on daily time series of the nine VOD products along with precipitation and NDVI at seven selected sites (Fig. 8, Table 3). In general, LPDR V2 X-VOD was found to show smoother daily variations than the other VOD products over all sites. It is also observed that SMOS-IC V2 VOD has a strongly reduced high frequency variability compared to its previous version (V105), especially in dense vegetation, for example over the evergreen broadleaf forest site in the Congo basin (Fig. 8a) and the mixed forests site over Mexico (Fig. 8b). This is because SMOS-IC adopted in V2 a new constraint method accounting for the fact that L-VOD has relatively low variations over short time periods (Wigneron et al., 2000). Consistent temporal patterns were found between most VOD products and NDVI at sites with low vegetation density, e.g. the savannas site over Brazil (Fig. 8c), the open shrublands site over south Australia (Fig. 8d) and the croplands site over Nigeria (Fig. 8e). An interesting feature of the time series is that some relatively small but distinct fluctuations in most VODs can be visually related to rainfall events; some examples are the December 2015 rainfall event at the savannas site, the November 2015 rainfall event at the open shrublands site, the January 2017 rainfall event for the grasslands site. These rainfall-related VOD variations could be a result from canopy-intercepted water and/or from changes in the vegetation water status due to the increase in the soil moisture availability (Feldman et al., 2018; Saleh et al., 2006).

Generally, for all sites, all VOD products and NDVI show a clear seasonality, i.e. increases during the vegetation growing season and decreases in the senescence period. However, this pattern is more or less pronounced depending on the sites and products, and some interesting features over the different sites are described below: At the evergreen broadleaf forest site, all L-VOD products, LPRM V5 C1- and C2-VOD, and LPDR V2 X-VOD show more dynamic variations in comparison with the LPRM V5 X-VOD, VODCA X- and C-VOD, and NDVI time series. However, even so, it seems that the seasonal change in VOD for LPRM V5 C1- and C2-band, and LPDR V2 X-band is less stable than that of the L-VOD products. Such a result was also found over the mixed forests site. These signatures may result from the saturation effects in the high frequency VOD values (see Section 4.3) in densely vegetated regions, which in turn lead to increased uncertainty in the retrievals. Over the savannas site in Brazil, the seasonal dynamics in all VODs and NDVI are very consistent and highly correlated (e.g. R values between 16-day averaged VOD of SMOS-IC V2 and NDVI is 0.94).

At the open shrublands site, a sudden decrease of AMSR2 LPRM V5 C1- and C2- VOD is observed at the end of February 2016, which is abnormal (seen as well in the Hovmöller diagrams Fig. 4). Ignoring this period, over that site, we found that most products could detect the relatively small but distinct fluctuations of VOD due to increased precipitation, whereas the LPDR V2 X-VOD time series failed to do so; for instance this can be noted for rainfall events that occurred in December 2016, January 2017, and March 2017. In the case of the croplands site, all VODs were found to lag with NDVI by ~16 days for LPDR V2 X-VOD and both versions of SMOS-IC L-VODs, and of ~30 days for the other VODs. A similar behavior is also observed, at the grasslands site, although less pronounced. All these results are consistent with Lawrence et al. (2014), who found that the SMOS L-VOD values (which are more related to the whole vegetation canopy including leaves, stems and fruits/grains) generally peaked later than the MODIS LAI values (more related to the vegetation green fraction) with an estimated time difference of about 19 days over crop zones of the USA.

4.3. Evaluating VOD against aboveground biomass

Density scatter plots of VOD-AGB relationships for the nine VOD products at the global scale reveal (1) an obvious non-linear saturating relationship between VOD and AGB, and (2) less pronounced saturation for L-VOD (Fig. 9). The spatial correlation of the relationship between VOD and AGB is ~0.80 for the L-VODs and between 0.61 and 0.67 for X-VODs and C-VODs, respectively. At X-band, VOD obtained from
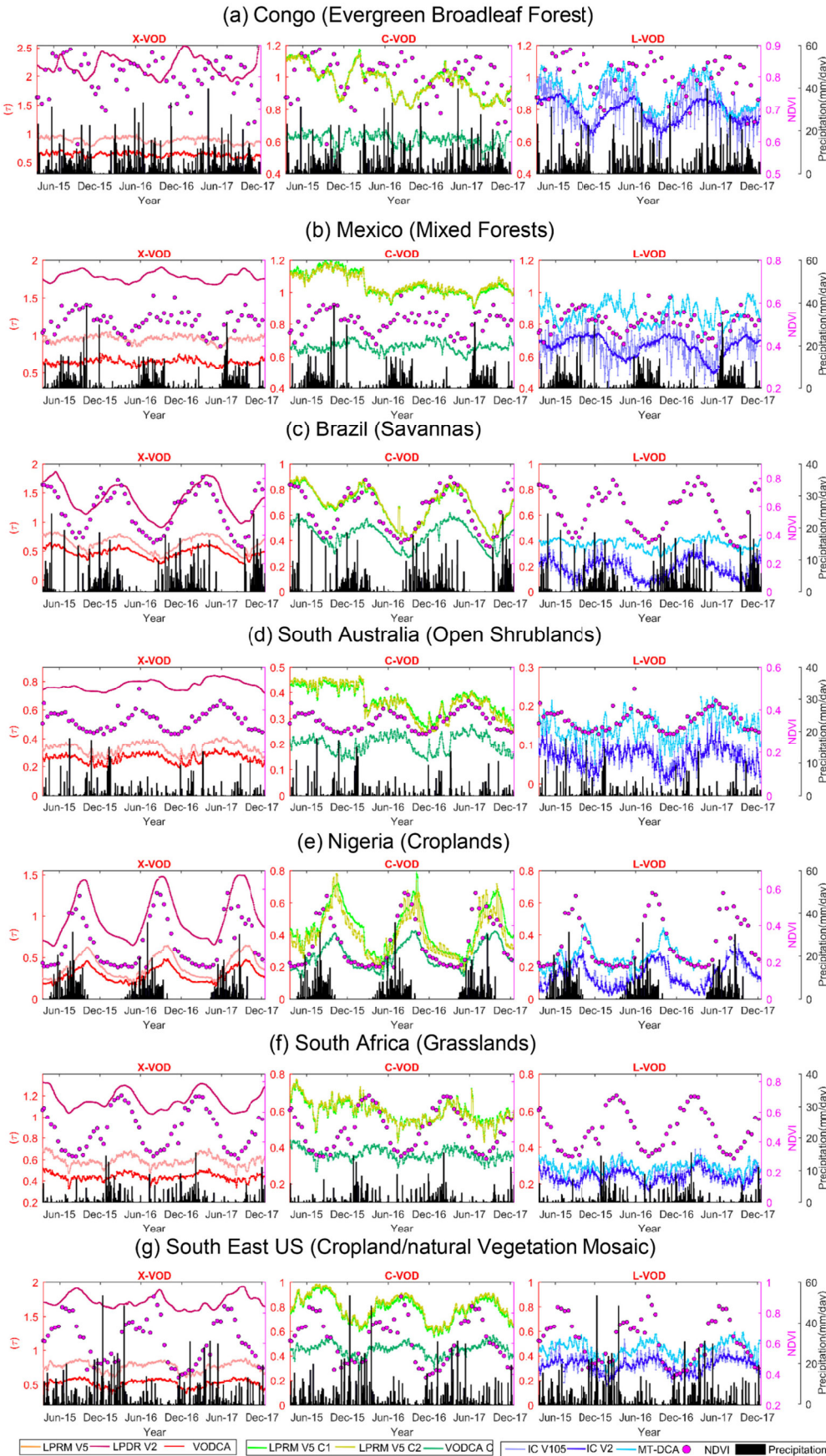
Fig. 8. Time series of the nine VOD products (smoothed with a moving window filter of seven days) at X-, C- and L-bands at selected sites from April 2015 to December 2017. Each plot also includes NDVI (shown in magenta dots; axis on the right) and daily precipitation (mm/day, shown in black; axis on the rightmost side) observed during the same period. Note: for completeness, Fig. 8a used data without quality control for LPDR VOD. (For interpretation of the references to colour in this figure legend, the reader is referred to the web version of this article.)
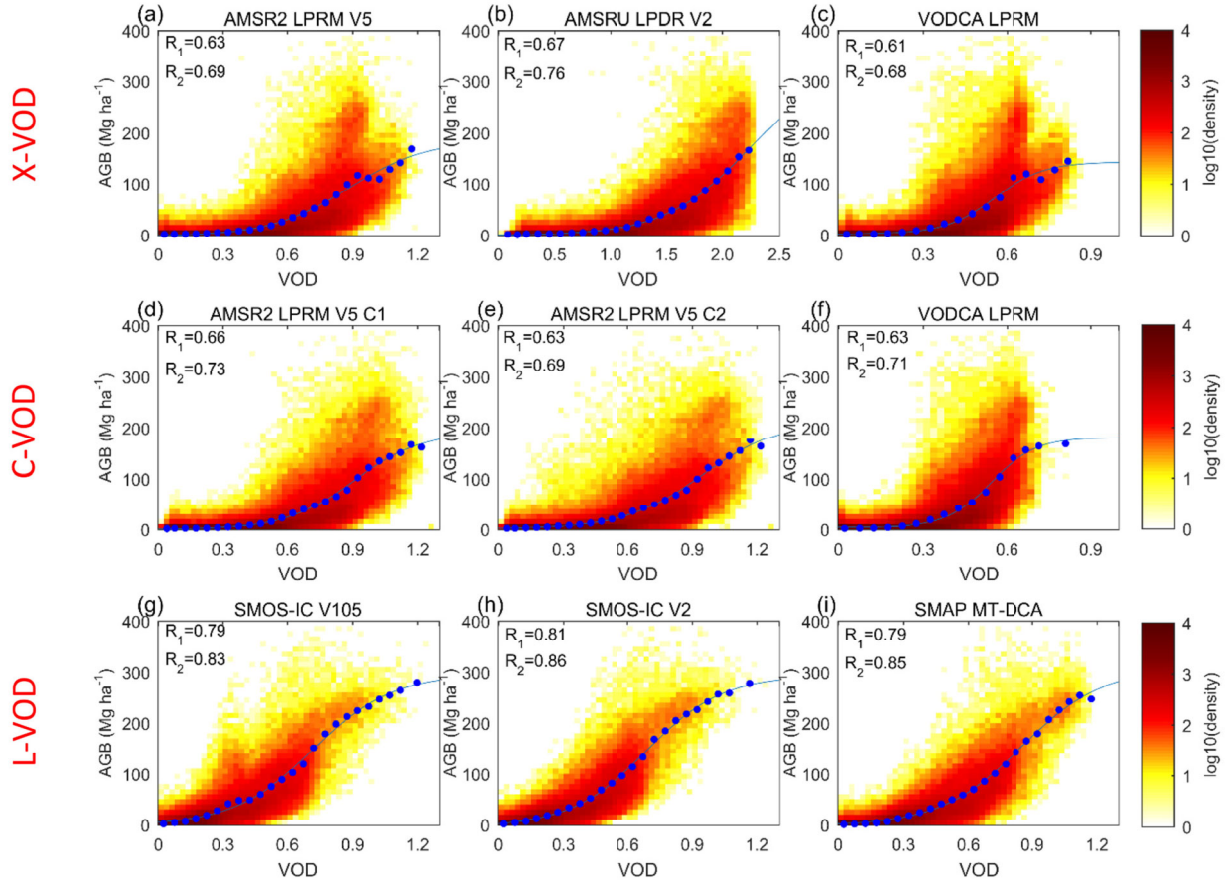
Fig. 9. Density scatter plots showing the spatial relationship between time averaged VOD at X-, C- and L-bands with AGB values. The mean AGB distribution in bins of VOD are displayed as blue circles, while solid blue lines are the fits obtained using a logistic function (Eq. 1). R_1 represents the spatial correlation between VOD and AGB, while R_2 represents the relationship between predicted AGB and reference AGB. All regressions are significant (*p*-value <0.001, the best-fit parameters are shown in Table S5). (For interpretation of the references to colour in this figure legend, the reader is referred to the web version of this article.)

reprocessed VODCA and AMSR2 LPRM V5 showed a similar dispersion and distribution shape, and the correlation values with AGB are lower than that obtained with LPDR V2 (Fig. 9a–c). At C-band, unlike LPRM V5 C1-band and C2-band which have a gradually smooth slope transition, the reprocessed VODCA VOD has a steep increase near AGB ~ 50 Mg ha^{-1} (VOD ~ 0.3) (Fig. 9d–f). At L-band, the shape of the density distribution obtained with SMOS-IC V2 has less distortion around VOD ~ 0.3 and AGB ~ 120 Mg ha^{-1} compared to V105, similar as SMAP MT-DCA (Fig. 9g–i). Notably, low-frequency L-VODs exhibit a high sensitivity to AGB, with a smooth relationship and without strong signs of saturation, which is not the case for high-frequency X-VODs and C-VODs.

Using the logistic function fitting (Section 3.2), both SMOS-IC V2 and SMAP MT-DCA L-VODs predict surface AGB very well, with a correlation

(R) of ~0.85 computed between predicted and observed AGB (Fig. 9). Best results were obtained from L-VODs followed by X-band LPDR V2 (*R*=0.76), which performed better than the other X-band products (i.e., AMSR2 LPRM V5 and VODCA LPRM X-VOD) and the C-band products. To achieve a fair comparison, we used identical pixels for the nine products at X-, C- and L-bands, filtering out many pixels corresponding to evergreen broadleaf forest (EBF) in tropical regions. This filtering was particularly due to the LPDR V2 X-VOD product, which includes many regions with no data in the tropical area after quality control (Fig. 2b) (such data gaps do not appear in the other VODs). This filtering leads to an underestimation in the ability of the other products (e.g., L-VOD) to estimate AGB. So, in a second step, we removed LPDR V2 from the comparison (the number of pixels increased by 8446 (6.02%) for the remaining comparisons), and the spatial correlation and prediction

Table 5
Spatial correlation of the nine VOD products at X-, C- and L-bands with AGB for different IGBP land cover classes.

Frequency	Product	ENF	EBF	DNF	DBF	MF	SH	WS	S	G	C	CNVM	B	R_total	R_estimate
X-VOD	AMSR2 LPRM V5	0.28	0.22	0.36	0.26	0.38	0.66	0.34	0.48	0.56	0.49	0.57	0.34	**0.63(0.66)**	**0.69(0.75)**
	AMSRU LPDR V2	0.14	0.19	0.40	0.25	0.41	0.68	0.44	0.52	0.54	0.51	0.63	0.37	**0.67 (×)**	**0.76 (×)**
	VODCA LPRM	0.24	0.16	0.38	–	0.38	0.66	0.33	0.46	0.55	0.45	0.54	0.36	**0.61(0.64)**	**0.68(0.73)**
C-VOD	AMSR2 LPRM V5 C1	0.31	0.32	0.42	0.28	0.40	0.68	0.40	0.51	0.58	0.51	0.58	0.28	**0.66(0.73)**	**0.73(0.84)**
	AMSR2 LPRM V5 C2	0.34	0.36	0.42	0.42	0.44	0.67	0.34	0.46	0.58	0.44	0.52	0.26	**0.63(0.71)**	**0.69(0.81)**
	VODCA LPRM C	0.32	0.28	0.34	–	0.35	0.64	0.34	0.39	0.56	0.47	0.54	0.35	**0.63(0.68)**	**0.71(0.78)**
L-VOD	SMOS-IC V105	0.37	0.59	0.66	0.54	0.18	0.73	0.53	0.63	0.63	0.61	0.73	0.39	**0.79(0.86)**	**0.83(0.90)**
	SMOS-IC V2	0.41	0.61	0.63	0.57	0.34	0.72	0.59	0.63	0.64	0.67	0.74	0.39	**0.81(0.88)**	**0.86(0.92)**
	SMAP MT-DCA	0.47	0.61	0.66	0.55	0.50	0.73	0.59	0.59	0.65	0.68	0.69	0.41	**0.79(0.85)**	**0.85(0.91)**

Note: [−] indicates that correlation is not significant (p-value>0.05). The number in brackets indicates the comparison result after removing LPDR V2 (the number of pixels increased from 140,302 to 148,748 (6.02%)).

ability of the reprocessed VODCA was found to be slightly lower than LPRM V5 at both X-band and C-band when compared with AGB (results in parentheses in Table 5 and in Fig. S7). In summary, the sensitivity of all the VODs to AGB follows the order L-VOD > C-VOD > X-VOD and the correlation between predicted AGB and observed AGB decreases from R ~ 0.92 to ~0.73 as the frequency increases.

All nine VOD products were found to have the highest spatial R values with AGB for shrublands (Table 5). However, after removing LPDR V2 which has more data gaps, a comparably high R value for evergreen broadleaf forest was obtained for L-VODs (Table S6). Lower R values for X-VODs and C-VODs were generally found over forest biomes. At X-band, both LPRM V5 and VODCA showed a higher R value with AGB than LPDR V2 for evergreen needleleaf forest and grasslands, while it was the opposite for the other IGBP types. At C-band, LPRM V5 C1-VOD (or VODCA C-VOD) was found to have the lowest (or non-significant) R value over deciduous broadleaf forest. Interestingly, the correlation obtained by LPRM V5 C2-band (7.3 GHz) was higher than that obtained by C1-band (6.9 GHz) over most forest types, while the opposite result was found over the short vegetation types (Table 5). More generally, for most vegetation types, VODCA VOD shows slightly lower R values than LPRM V5. For low frequency L-VOD, higher R values were obtained for SMOS-IC V2 *vs.* V105 over most vegetation types, while the R values obtained by both versions of SMOS-IC were lower than those of SMAP MT-DCA over mixed forests. As expected, due to the improved propagation capabilities of the microwave radiations as the frequency decreases, the spatial correlation between VOD and AGB increased with decreasing frequency, and this feature is more obvious in dense forests, even from X-band to C-band (except VODCA VOD). However, for short vegetation, although the L-band still has the leading edge, results obtained at X-bands are very good and almost comparable to those obtained with C-VODs, in particular over woody savannas, savannas and cropland/natural vegetation mosaic.

5. Discussion

The results presented in this study have implications in two main fields. First, we revealed specific features and deficiencies in the VOD products that may provide useful hints for the remote sensing community dedicated to VOD retrieval improvements. Second, our results may be useful for the research community more dedicated to the use of the VOD products for vegetation monitoring. These two main types of implications are discussed in the following sections.

5.1. Possible ways to improve the VOD retrievals

The analysis of the different results obtained in this study revealed specific features or deficiencies of some products:

(i) For LPRM V5 products, the magnitude of X-VOD < C-VOD over some dense forests (Fig. 2 and Fig. 3) does not meet the theoretical principle that the penetration of microwave radiations within the vegetation canopy should decrease with frequency due to increasing extinction effects;

(ii) LPDR V2 X-VOD time series failed to detect changes in VOD after rainfall events (Fig. 8) whereas most VOD products could do so, and overall LPDR V2 X-VOD has smoother daily variations;

(iii) The MT-DCA approach for SMAP has lower correlation with optical datasets (NDVI, EVI) than SMOS-based L-band products (Fig. 8 and Table S4);

(iv) The spatial correlations between L-VODs and MODIS VIs were found to be lower than those of C- and X-VODs particularly over grasslands and croplands (Table 4), while all VODs have comparable performances over the other relatively short vegetation IGBP types.

(v) C- and X-VODs have a comparable or even higher spatial correlation with respect to canopy height than L-VODs over evergreen

needleleaf forest and mixed forests (Table S2). This relative deficiency of the L-VODs was noted particularly in boreal regions.

All these findings indicate that there is some margin to improve the current VOD products or algorithms, but also keeping in mind their field of application. Concerning deficiencies (i), the evaluation/calibration of the model parameters (e.g., roughness (HR) and effective scattering albedo (ω)) may need to be reconsidered to develop improved products. Considering the calibration of ω, divergences could be noted in different studies. For instance, Baur et al. (2019) found that ω decreased slightly with frequency or showed highest values at C-band when retrieving simultaneously VOD and ω at X-, C-, and L-bands. However, the setting of ω in the LPRM V5 algorithm is reversed (the calibrated value of ω is increasing with frequency) (Table 2). Uncertainties associated with the roughness and ω parameters affect all VOD products, not just those from LPRM - there is still no consensus on how the roughness parameters change with frequency (even though Wigneron et al. (2017) found these changes are relatively low), and how these changes affect the VOD retrievals at different frequencies. Indeed, differing assumptions for the values of these ancillary parameters may also explain the very different magnitudes of the X-VOD values between the LPDR and LPRM datasets (although these could also be caused by differing corrections for the effects of open water bodies and land surface temperature between the datasets). In addition, the HR roughness parameter may also have a considerable effect on the retrieved values of VOD, SM and ω (Fernandez-Moran et al., 2017a, 2017b; Karthikeyan et al., 2019). For instance, at L-band, changes in roughness can be partially accounted for by changes in L-VOD, leading to a low impact on the SM retrievals but a strong impact on L-VOD (Hornbuckle et al., 2017; Parrens et al., 2016).

Issues (ii) and (iii) are both related to assumptions made in the algorithm development. For instance, the LPDR algorithm assumes a constant dry bare soil emissivity in the VOD retrievals (Table 2), which may balance/ignore the impact of rainfall on the simulated TB in the original τ-ω equation (Du et al., 2017a, 2017b). Another possible reason is that a 30-day moving median filter is applied to its daily VOD values (Jones et al., 2011), which also makes its time series smoother than for the other products in Fig. 8. As for SMAP, to solve the under-determined retrieval problem of the dual-channel algorithm (DCA) from its single-angle TB, MT-DCA was developed assuming that VOD is constant over a time window. However, this assumption is likely to be violated especially over grasslands and croplands where vegetation growth can be very fast, e.g., the VOD value can increase by ~0.2 [−] per 10 days in a cornfield (Jackson et al., 2004), or right after a rain storm, when the relative vegetation water content increases quickly. Besides, the temporal changes of emissivity are not evenly distributed across the globe, which may also affect the performance of MT-DCA (Gao et al., 2020b). One possible way to improve the weak assumption in MT-DCA is to take into account the slow changes of VOD using a smooth-regularization technique (Gao et al., 2020a).

Issues (iv) and (v) could be partly related to the fact the IGBP classification used here does not match the study period, and pure biomes are also very rare in the 25 km land classification: in reality all pixels are more or less heterogeneous and include a variety of IGBP land vegetation types. On the other hand, it is likely issues (iv) and (v) revealed specific retrieval issues for some ecosystems, e.g., grasslands, croplands and boreal regions. Possible reasons are briefly discussed in the following. Grasslands exhibit complex microwave signatures at L-band, due to the presence of a thatched litter layer of dead grass under the green vegetation in non-plowed areas (Grant et al., 2016; Saleh et al., 2007). Such a thatched litter layer, particularly when it is wet, can have a large effect on the L-band emission and/or may lead to complex coherent scattering effects within the vegetation layer, for specific moisture status of the vegetation, litter and soil layers (Grant et al., 2009). These effects may be lower for high-frequency observations as the latter are more sensitive to the top-of-the-canopy layer. For croplands, changes in surface roughness due to farming practices may impact

the VOD retrievals (Fernández-Morán et al., 2015; Patton and Hornbuckle, 2012) and this impact may be more pronounced at L-band than at X- and C-bands for some specific soil/vegetation conditions (Montpetit et al., 2015).

In boreal regions, the VOD retrievals may be intricate due to specific features (e.g., open water bodies and frozen conditions) of the ecosystems in the northern regions. In the latter regions, large climatic variations support the existence of diverse conifer forests types, with very different tree densities with specific phenological behaviors, in particular for deciduous needleleaf forest (DNF) which are prevalent in east Siberia (Crowther et al., 2015). Moreover, both broadleaf and needleleaf species coexist in most boreal forests, making VOD temporal averaging delicate and temporal averaging can be only calculated over a limited period, since the data in winter are often affected by frozen/snow conditions. Furthermore, soils in the boreal regions are characterized by a high content of organic matter leading to distinct dielectric behaviors, as organic materials differ from the mineral ones by their complex structure, large specific surface area, high porosity and small bulk density (Wigneron et al., 2017). Such an effect is not considered in VOD retrieval algorithms (Table 2) and particularly in the two L-VOD retrieval algorithms (SMOS-IC and SMAP MT-DCA) which currently use the Mironov dielectric mixing model (Mironov et al., 2004) based only on the clay fraction. Thus, adopting a new dielectric model applicable to organic soils in boreal regions may be considered in future generations of the VOD retrieval algorithms (Mironov et al., 2019). Finally, the RFI impact is also very important in the boreal regions, especially at L-band (Al-Yaari et al., 2019).

5.2. Limitations of the evaluation approach

It should be noted that there are some limitations in the VOD evaluation made here that should be considered for a better interpretation of the results in VOD application studies. First, temporal correlation between VOD and optical VIs (Fig. 6 and Fig. 7) cannot be used as an "absolute" criterion for judging the quality of the different products as low or even negative temporal R values can be explained by a temporal lag between different climate and vegetation variables (SM, X/C/L-VOD, LAI, EVI) in some ecosystems (Jones et al., 2011). For instance, Jones et al. (2014) found that the period of canopy biomass growth (indicated by X-VOD), maximum water availability and net leaf flush in the Amazon forests are asynchronous and follow a gradient from west to east, which reveals the adaptability of the Amazon forests to water and light availability. Similarly, Tian et al. (2018) found that SMOS L-VOD lags the leaf development by up to ~180 days in dry tropical woodlands, explaining that L-VOD *vs.* optical VIs showed a negative correlation in some regions such as the large Miombo woodlands south of the Congo basin (Fig. 6g-i). A time lag of ~19 days between L-VOD and LAI was also found for crops in the USA (Lawrence et al., 2014), similarly to the site analysis presented in this study (Fig. 8e) (a time lag was found here for all the X-, C- and L-band VODs).

Additionally, the proxies we chose, MODIS VIs, Lidar tree height and AGB, although widely used in VOD evaluation studies (Fan et al., 2019; Liu et al., 2011; Rodríguez-Fernández et al., 2018), cannot be considered as "truth" (Li et al., 2020a). Moreover, the impact of daily or seasonal changes in the vegetation water status as considered in other fields of research by Konings et al. (2019) and Tian et al. (2018), were not evaluated/removed here when evaluating VOD against annual AGB maps. Similarly, averaging VOD retrievals to 16-day to analyze its ability to monitor the vegetation dynamics may also ignore some information observed by daily-scale VOD, e.g., pulse-reserve paradigm (Feldman et al., 2018). This latter topic would require a specific analysis based on other proxies of the vegetation water status and water stress (Konings et al., 2019) and will be considered in more focused future studies. Nevertheless, in spite of their limitations, we think the chosen proxies are relatively complementary in this study to evaluate VOD retrievals as (i) correlation with MODIS VIs could be regarded as a

criterion more pertinent for short vegetation canopies. We noted too that higher correlation values in both temporal and spatial terms and for most vegetation types were generally found between VOD and NDVI as compared to VOD and EVI; (ii) correlations with global tree height and biomass is considered relevant for woody vegetation types. In the future, triple collocation (TC) or TC-related methods may also be used to estimate the correlation metric of satellite vegetation optical products relative to unknown ground truth (Dong et al., 2019; Gruber et al., 2016), once an independent vegetation optical product is available (e.g., ASCAT active VOD; Liu et al., 2020).

6. Concluding remarks and outlook

In this study, the performance of nine recently developed/reprocessed microwave satellite VOD products at L-, C- and X- bands for monitoring vegetation features, were assessed and inter-compared in relation to seasonal change and of sensitivity to biomass at the global scale. The nine VODs were evaluated against MODIS VIs (i.e., NDVI and EVI), tree height, and AGB across different IGBP vegetation types. We found that:

(i) X-VODs, particularly in the LPDR version, have a stronger ability than C- and L- VODs to monitor seasonal changes in the green vegetation components in regions which are not densely vegetated, and they show higher temporal correlation values (R) with MODIS VIs (median R values of 0.74 at the global scale). More surprisingly, low frequency L-VOD, particularly the new SMOS-IC V2 version also shows high temporal correlation values with VIs similar to C-VODs in some biomes such as savannas (R ~ 0.70).

(ii) L-VODs which have stronger penetration capabilities within the vegetation canopies than high-frequency products, show a high spatial correlation with canopy height, with SMOS-IC V2 and SMAP MT-DCA showing similar scores at global scale (R ~ 0.90). Moreover, we reveal a good linear relationship with a low dispersion with respect to tree height, even in tall forests.

(iii) L-VODs are more sensitive to the non-green vegetation components (trunks and branches) than the higher frequency (i.e., X- and C-VOD) products, thus showing a high correlation with aboveground biomass. Logistic fitting function provided a correlation between predicted AGB and observed AGB of R ~ 0.91 for SMOS-IC V2 and SMAP MT-DCA L-VOD at a global scale.

Our results suggest that it may be very interesting to analyze the time lags of VODs computed at different frequencies and vegetation or climate variables, as it may help us to better understand the adaptability of the vegetation ecosystems to water and light availability and temperature conditions, as done by Jones et al. (2014) in the Amazon forests. Further studies can now be made, considering the availability of long-term and improved sequences of L-VODs, that can provide information on forest dynamics for deeper layers of the canopy, e.g., SMOS-IC L-VOD is now available for 10 years (Table 1). Moreover, VODs can be particularly useful in regions where the optical observations are affected by atmospheric and aerosol effects and by cloud cover, as VODs are retrieved independently of the optical-near infrared remote sensing-based VIs and are relatively insensitive to signal perturbation from sun-sensor illumination conditions and atmospheric effects. Conversely, optical VIs have a relatively higher spatial resolution and VOD and optical VIs may thus be used complementary. Their synergistic use could provide a more comprehensive assessment of dynamic vegetation features such as phenology (Jones et al., 2011) and carbon stocks (Chaparro et al., 2019).

We expect that our findings can contribute to improve the satellite vegetation optical depth retrieval algorithms by reporting on strengths and weaknesses of current VODs depending on the vegetation features (leaf development, structure, height and biomass). Our findings could also help selecting best suited VOD product depending on the

applications and contribute to promote the use of VODs for vegetation monitoring on the subjects of carbon stocks, vegetation dynamics and phenology.

Declaration of Competing Interest

The authors declare that they have no conflict of interest.

Appendix A. Remotely sensed VOD products

A.1. SMOS-IC (V105&V2)

The ESA's SMOS mission, which was launched on November 2, 2009, was the first L-band space-borne mission dedicated to monitoring global land soil moisture (Kerr et al., 2010). It is equipped with a microwave synthetic aperture radiometer (1.4 GHz) which can provide multi-angle and dual-polarized brightness temperature (TB) observations over a range of incidence angles ($\sim$ 0–60°). This observational feature allows to robustly infer properties of the soil and vegetation (i.e., retrieving SM and VOD) simultaneously from the SMOS data (Wigneron et al., 2017). In this context, to make efficient use of the TB observations (that is, to be as much as possible independent from auxiliary datasets), an alternative SMOS SM and VOD product (initially called SMOS-INRA-CESBIO or SMOS-IC) was developed and the first publicly released version was V105 (Fernandez-Moran et al., 2017a, 2017b). SMOS-IC has the main following features:

  i) independent of auxiliary data: contrary to the official algorithms no ECMWF modelled SM data or MODIS LAI products are used in SMOS-IC; only ECMWF temperature is used currently (Fernandez-Moran et al., 2017a; Li et al., 2020a);

  ii) relative to the baseline SMOS algorithms, it is simpler and avoids uncertainties and errors associated with inconsistent auxiliary datasets and decision trees which are adopted to characterize the pixel heterogeneity in the other SMOS algorithms (Wigneron et al., 2018);

  iii) it is based on new maps of model parameters for soil roughness and vegetation scattering effects (Fernandez-Moran et al., 2017a; Parrens et al., 2016).

All the above features make SMOS-IC products very performant compared to other products for both SM (Al-Yaari et al., 2019; Dong et al., 2020; Ma et al., 2019; Sadeghi et al., 2020) and VOD (Rodríguez-Fernández et al., 2018). For instance, in terms of SM, recent inter-comparison studies have shown that the SMOS-IC SM product is very accurate and close to the performances of SMAP (Al-Yaari et al., 2019), and possibly reaching best performances over dense vegetation canopies (Ma et al., 2019). In terms of VOD, the SMOS-IC VOD products have been found to provide more accurate relationships than the CATDS (Centre Aval de Traitements des Données SMOS) official SMOS products to estimate above ground biomass (Rodríguez-Fernández et al., 2018). The SMOS-IC VOD products have been increasingly used over the very recent years in a number of applications, such as monitoring vegetation

seasonality (Tian et al., 2018), crop modelling (Chaparro et al., 2018), and carbon cycle (Bastos et al., 2020; Brandt et al., 2018; Fan et al., 2019; Wigneron et al., 2020), etc.

Since the release of the first version V105, several improvements have been applied to the SMOS-IC algorithm, leading to the production of the version 2 (V2), based on a collaboration between INRAE and China Scholarship Council. A major improvement concept is that VOD has low time variations over short time periods (Tian et al., 2018; Wigneron et al., 2007), which was not properly considered in V105. To implement this concept, the optimization processing of the a priori information on VOD to constrain the retrievals has been modified in SMOS-IC V2: to retrieve VOD at a date t, previously retrieved VOD values (over a period of 10 days before date t) are used to initialize the first guess value of VOD (VOD^{ini}) in the cost function. Readers are referred to Wigneron et al. (Submitted) for more detailed description of the SMOS-IC V2 retrieval algorithm. It should be noted that the improvements in SMOS-IC V2 are obvious for both SM and VOD. As the focus of this study is VOD, the assessment of SM is not presented here (Li et al., 2020b; Wigneron et al., Submitted).

Both versions of SMOS-IC products are projected on a global Equal Area Scalable Earth Grid version 2 (EASE-Grid 2.0), and the SM datasets of V105 are available in the Network Common Data Form (NetCDF) format through CATDS for both ascending (6:00 am) and descending (6:00 pm) orbits with a spatial resolution of 25 km. In this study, we used both versions of SMOS-IC VOD retrieved using observations acquired from the ascending orbits, at early morning, which are less sensitive to the vegetation water status than observations acquired in the afternoon from the descending orbits.

A.2. SMAP MT-DCA

The NASA's SMAP mission, which was launched on January 31, 2015, is the most recent L-band space-borne satellite for global soil moisture and landscape freeze/thaw state mapping (Entekhabi et al., 2010). Since the radar instrument (1.26 GHz) failed after about 11 weeks of operation, SMAP has only relied on the passive radiometer (1.41 GHz) to collect fully-polarized TB operating at a single incidence angle of 40°. This single-angle configuration limits the robustness of retrievals of both SM and VOD from a dual-channel algorithm (DCA) as the Horizontal (H-) and Vertical (V-) polarized TB observations contain some shared information (O'Neill et al., 2015; Konings et al., 2016). After comparing several algorithms, the driving SM inversion algorithm of the SMAP mission is a single-channel algorithm (Jackson, 1993) based on V polarization (SCA-V), which NDVI data is used as ancillary information to estimate VOD in the retrieval process (Chan et al., 2013). In contrast, by considering multi-temporal (MT-) observation information in the DCA approach, a new algorithm called MT-DCA was developed for simultaneously retrievals of SM, VOD and effective scattering albedo without using ancillary datasets on vegetation (Konings et al., 2016, 2017). One of the main assumptions of MT-DCA is that the temporal variations of VOD is slower than that of SM and the values of VOD are assumed to be almost constant for two consecutive overpasses. Readers are referred to Konings et al. (2016, 2017) for more information about this algorithm.

The latest SMAP MT-DCA (V4) L-VOD including 9 km and 36 km is available in a binary format (.mat) on a global EASE-Grid 2.0 through http://afeldman.mit.edu/mt-dca-data. In this study, we used the 9 km SMAP MT-DCA L-VOD covering about 2 years and a half (see Section 3.1). This dataset was retrieved from the SMAP Level 1C Enhanced Brightness Temperature Product (L1C_TB_E) with the descending orbit (6:00 AM) as input.

A.3. AMSR2 (LPRM&LPDR)

The AMSR2, which was launched by JAXA on May 17, 2012, is an improved successor of AMSR-E onboard GCOM-W1. AMSR2 has similar

orbits, bands and local overpass times (1:30 am for descending orbit and 1:30 pm for ascending orbit) as AMSR-E (Imaoka et al., 2012). In addition, it also includes a second C-band channel (C2-band, 7.3 GHz), which can be applied to cover areas where RFI exists in the main C1-band channel (6.9 GHz). In this study we used AMSR2 VOD products for the descending orbits computed from two reference algorithms (i) LPRM (Land Parameter Retrieval Model; Owe et al., 2008) and (ii) LPDR (Land Parameter Data Record; Du et al., 2017b). These AMSR2 VOD products have the same sample resolution of 25 km and are briefly described in the following.

In the LPRM algorithm, based on the 0th-order Tau-Omega emission model (Mo et al., 1982), both SM and VOD are obtained simultaneously from the Microwave Polarization Difference Index (MPDI) with the use of an analytical retrieval methodology (Meesters et al., 2005). In the present study, we used the AMSR2 VOD product retrieved from LPRM V5 (Owe et al., 2008), as the latest version (V6) is not publicly available (van der Schalie et al., 2017). The LPRM V5 retrieval process used AMSR2 spatial-resolution-matched TB (L1SGRTBR) as input TB data, and the input land surface temperature was retrieved separately from the AMSR2 Ka-band (36.5 GHz; Holmes et al., 2009). Here, we used the descending VOD products from AMSR2 C1-, C2-, X-band (Vrije Universiteit Amsterdam and NASA GSFC, 2014).

The LPDR version 2 (V2) is an enhanced data record over prior (V1) LPDR, in which X-band VOD is obtained by inverting the land-water microwave emissivity slope index (Du et al., 2017b). In comparison to the previous version (Jones et al., 2010), V2 has advantages in both temporal coverage and retrieval accuracy, and the main refinements and updates include: i) extended time period from AMSR-E (June 19, 2002) to AMSR2 (December 31, 2018) by empirically calibrating the AMSR2 multi-frequency TB retrieval algorithm on the same channel as AMSR-E; ii) refined AMSR2 estimation of the daily maximum and minimum surface air temperature by considering terrain and latitude effects (Du et al., 2015); iii) improved SM retrieval by using a dynamic selection of vegetation-scattering albedos (Du et al., 2016). We refer readers to Du et al. (2017b) for further detailed information on this algorithm. The LPDR V2 X-VOD is projected on global EASE-Grid (V1) with a GeoTIFF format and is freely available via (https://nsidc.org/data/nsidc-0451).

A.4. VOD Climate Archive (VODCA)

The TU Wien's VODCA product, which combined multiple single-sensor VOD retrievals derived using LPRM algorithm, is a global daily VOD product with a sampling resolution of 0.25 degrees (Moesinger et al., 2020). This product was inspired by Liu's long-term (1987–2008) harmonized multi-sensor VOD dataset (Liu et al., 2011) and ESA's first long-term satellite-based climate data record of soil moisture within the Climate Change Initiative (ESA CCI SM; Gruber et al., 2019). It is based on a similar core methodology as Liu et al. (2011) but incorporates new insights into VOD and the strategies in the production of ESA CCI SM climate data records in recent years (Moesinger et al., 2020). Specifically, unlike Liu et al. (2011), which harmonized all observations to AMSR-E's high-quality C-VOD, this product is a frequency-specific VOD dataset as different frequencies carry valuable specific information suitable for various applications (Teubner et al., 2019). VODCA combined VOD observations from AMSR2, WindSat, AMSR-E, Tropical Rainfall Measuring Mission (TMI), and Special Sensor Microwave/Imager (SSM/I) into long-term VOD datasets at C-band (period 2002–2018), X-band (1997–2018), and Ku-band (1987–2017). The biases between the VOD values retrieved from different sensors were eliminated by scaling them to AMSR-E VOD using a new implementation of the cumulative distribution function matching technique; further detailed information about the retrieval algorithm are given in Moesinger et al. (2020). In this study, we only used VODCA X- and C-VOD, as the Ku-VOD products were incomplete in 2017 (no data from August to December).

Appendix B. Supplementary data

Supplementary data to this article can be found online at https://doi.org/10.1016/j.rse.2020.112208.

References

Al-Yaari, A., Wigneron, J.P., Ducharne, A., Kerr, Y., de Rosnay, P., de Jeu, R., Govind, A., Al Bitar, A., Albergel, C., Muñoz-Sabater, J., Richaume, P., Mialon, A., 2014. Global-scale evaluation of two satellite-based passive microwave soil moisture datasets (SMOS and AMSR-E) with respect to land data assimilation system estimates. Remote Sens. Environ. 149, 181–195.

Al-Yaari, A., Wigneron, J.P., Dorigo, W., Colliander, A., Pellarin, T., Hahn, S., Mialon, A., Richaume, P., Fernandez-Moran, R., Fan, L., Kerr, Y.H., De Lannoy, G., 2019. Assessment and inter-comparison of recently developed/reprocessed microwave satellite soil moisture products using ISMN ground-based measurements. Remote Sens. Environ. 224, 289–303.

Asner, G.P., Clark, J.K., Mascaro, J., García, G.G., Chadwick, K.D., Encinales, D.N., Paez-Acosta, G., Montenegro, E.C., Kennedy-Bowdoin, T., Duque, Á., 2012. High-resolution mapping of forest carbon stocks in the Colombian Amazon. Biogeosciences 9, 2683.

Bastos, A., Ciais, P., Friedlingstein, P., Sitch, S., Pongratz, J., Fan, L., Wigneron, J., Weber, U., Reichstein, M., Fu, Z., 2020. Direct and seasonal legacy effects of the 2018 heat wave and drought on European ecosystem productivity. Sci. Adv. 6, eaba2724.

Baur, M.J., Jagdhuber, T., Feldman, A.F., Akbar, R., Entekhabi, D., 2019. Estimation of relative canopy absorption and scattering at L-, C- and X-bands. Remote Sens. Environ. 233, 111384.

Brandt, M., Wigneron, J.P., Chave, J., Tagesson, T., Penuelas, J., Ciais, P., Rasmussen, K., Tian, F., Mbow, C., Al-Yaari, A., Rodriguez-Fernandez, N., Schurgers, G., Zhang, W., Chang, J., Kerr, Y., Verger, A., Tucker, C., Mialon, A., Rasmussen, L.V., Fan, L., Fensholt, R., 2018. Satellite passive microwaves reveal recent climate-induced carbon losses in African drylands. Nat. Ecol. Evol. 2, 827–835.

Brandt, M., Hiernaux, P., Rasmussen, K., Tucker, C.J., Wigneron, J.P., Diouf, A.A., Herrmann, S.M., Zhang, W.M., Kergoat, L., Mbow, C., Abel, C., Auda, Y., Fensholt, R., 2019. Changes in rainfall distribution promote woody foliage production in the Sahel. Commun. Biol. 2, 1–10.

Broxton, P.D., Zeng, X., Sulla-Menashe, D., Troch, P.A., 2014. A global land cover climatology using MODIS data. J. Appl. Meteorol. Climatol. 53, 1593–1605.

Carreiras, J.M., Quegan, S., Le Toan, T., Minh, D.H.T., Saatchi, S.S., Carvalhais, N., Reichstein, M., Scipal, K., 2017. Coverage of high biomass forests by the ESA BIOMASS mission under defense restrictions. Remote Sens. Environ. 196, 154–162.

Chan, S., Bindlish, R., Hunt, R., Jackson, T., Kimball, J., 2013. Soil Moisture Active Passive (SMAP) Ancillary Data Report: Vegetation Water Content. Pasadena, California.

Chaparro, D., Piles, M., Vall-Llossera, M., Camps, A., Konings, A.G., Entekhabi, D., 2018. L-band vegetation optical depth seasonal metrics for crop yield assessment. Remote Sens. Environ. 212, 249–259.

Chaparro, D., Duveiller, G., Piles, M., Cescatti, A., Vall-llossera, M., Camps, A., Entekhabi, D., 2019. Sensitivity of L-band vegetation optical depth to carbon stocks in tropical forests: a comparison to higher frequencies and optical indices. Remote Sens. Environ. 232, 111303.

Crowther, T.W., Glick, H.B., Covey, K.R., Bettigole, C., Maynard, D.S., Thomas, S.M., Smith, J.R., Hintler, G., Duguid, M.C., Amatulli, G., 2015. Mapping tree density at a global scale. Nature 525, 201–205.

Cui, T., Sun, R., Xiao, Z., Liang, Z.Y., Wang, J., 2020. Simulating spatially distributed solar-induced chlorophyll fluorescence using a BEPS-SCOPE coupling framework. Agric. For. Meteorol. 295, 108169.

Dobson, M.C., Ulaby, F.T., Hallikainen, M.T., El-Rayes, M.A., 1985. Microwave dielectric behavior of wet soil-part II: dielectric mixing models. IEEE Trans. Geosci. Remote Sens. 35–46.

Dong, J., Crow, W.T., Bindlish, R., 2018. The error structure of the SMAP single and dual channel soil moisture retrievals. Geophys. Res. Lett. 45, 758–765.

Dong, J., Crow, W.T., Duan, Z., Wei, L., Lu, Y., 2019. A double instrumental variable method for geophysical product error estimation. Remote Sens. Environ. 225, 217–228.

Dong, J., Crow, W.T., Tobin, K.J., Cosh, M.H., Bosch, D.D., Starks, P.J., Seyfried, M., Collins, C.H., 2020. Comparison of microwave remote sensing and land surface modeling for surface soil moisture climatology estimation. Remote Sens. Environ. 242, 111756.

Du, J., Kimball, J.S., Jones, L.A., 2015. Satellite microwave retrieval of Total Precipitable water vapor and surface air temperature over land from AMSR2. IEEE Trans. Geosci. Remote Sens. 53, 2520–2531.

Du, J., Kimball, J.S., Jones, L.A., 2016. Passive microwave remote sensing of soil moisture based on dynamic vegetation scattering properties for AMSR-E. IEEE Trans. Geosci. Remote Sens. 54, 597–608.

Du, J., Jones, L., Kimball, J., 2017a. Daily Global Land Parameters Derived from AMSR-E and AMSR2 (Version 2.0). National Snow Ice Data Center, Boulder, CO, USA.

Du, J., Kimball, J.S., Jones, L.A., Kim, Y., Glassy, J., Watts, J.D., 2017b. A global satellite environmental data record derived from AMSR-E and AMSR2 microwave earth observations. Earth Syst. Sci. Data 9, 791–808.

Entekhabi, D., Njoku, E.G., O'Neill, P.E., Kellogg, K.H., Crow, W.T., Edelstein, W.N., Entin, J.K., Goodman, S.D., Jackson, T.J., Johnson, J., 2010. The soil moisture active passive (SMAP) mission. Proc. IEEE 98, 704–716.

Fan, L., Wigneron, J.P., Ciais, P., Chave, J., Brandt, M., Fensholt, R., Saatchi, S.S., Bastos, A., Al-Yaari, A., Hufkens, K., Qin, Y., Xiao, X., Chen, C., Myneni, R.B., Fernandez-Moran, R., Mialon, A., Rodriguez-Fernandez, N.J., Kerr, Y., Tian, F., Penuelas, J., 2019. Satellite-observed pantropical carbon dynamics. Nat. Plants 5, 944–951.

Feldman, A.F., Short Gianotti, D.J., Konings, A.G., McColl, K.A., Akbar, R., Salvucci, G. D., Entekhabi, D., 2018. Moisture pulse-reserve in the soil-plant continuum observed across biomes. Nat. Plants 4, 1026–1033.

Fernández-Morán, R., Wigneron, J.-P., Lopez-Baeza, E., Al-Yaari, A., Coll-Pajaron, A., Mialon, A., Miernecki, M., Parrens, M., Salgado-Hernanz, P.M., Schwank, M., 2015. Roughness and vegetation parameterizations at L-band for soil moisture retrievals over a vineyard field. Remote Sens. Environ. 170, 269–279.

Fernandez-Moran, R., Al-Yaari, A., Mialon, A., Mahmoodi, A., Al Bitar, A., De Lannoy, G., Rodriguez-Fernandez, N., Lopez-Baeza, E., Kerr, Y., Wigneron, J.-P., 2017a. SMOS-IC: an alternative SMOS soil moisture and vegetation optical depth product. Remote Sens. 9.

Fernandez-Moran, R., Wigneron, J.P., De Lannoy, G., Lopez-Baeza, E., Parrens, M., Mialon, A., Mahmoodi, A., Al-Yaari, A., Bircher, S., Al Bitar, A., Richaume, P., Kerr, Y., 2017b. A new calibration of the effective scattering albedo and soil roughness parameters in the SMOS SM retrieval algorithm. Int. J. Appl. Earth Obs. Geoinf. 62, 27–38.

Frappart, F., Wigneron, J.-P., Li, X., Liu, X., Al-Yaari, A., Fan, L., Wang, M., Moisy, C., Le Masson, E., Aoulad Lafkih, Z., Vallé, C., Ygorra, B., Baghdadi, N., 2020. Global monitoring of the vegetation dynamics from the vegetation optical depth (VOD): a review. Remote Sens. 12, 2915.

Gao, L., Sadeghi, M., Ebtehaj, A., 2020a. Microwave retrievals of soil moisture and vegetation optical depth with improved resolution using a combined constrained inversion algorithm: application for SMAP satellite. Remote Sens. Environ. 239, 111662.

Gao, L., Sadeghi, M., Ebtehaj, A., Wigneron, J.-P., 2020b. A temporal polarization ratio algorithm for calibration-free retrieval of soil moisture at L-band. Remote Sens. Environ. 249, 112019.

Grant, J.P., Van de Griend, A.A., Schwank, M., Wigneron, J.-P., 2009. Observations and modeling of a pine forest floor at L-band. IEEE Trans. Geosci. Remote Sens. 47, 2024–2034.

Grant, J.P., Wigneron, J.P., De Jeu, R.A.M., Lawrence, H., Mialon, A., Richaume, P., Al Bitar, A., Drusch, M., van Marle, M.J.E., Kerr, Y., 2016. Comparison of SMOS and AMSR-E vegetation optical depth to four MODIS-based vegetation indices. Remote Sens. Environ. 172, 87–100.

Gruber, A., Su, C.H., Crow, W.T., Zwieback, S., Dorigo, W.A., Wagner, W., 2016. Estimating error cross-correlations in soil moisture data sets using extended collocation analysis. J. Geophys. Res. Atmos. 121, 1208–1219.

Gruber, A., Scanlon, T., van der Schalie, R., Wagner, W., Dorigo, W., 2019. Evolution of the ESA CCI soil moisture climate data records and their underlying merging methodology. Earth Syst. Sci. Data 1–37.

Guan, K., Wood, E.F., Caylor, K.K., 2012. Multi-sensor derivation of regional vegetation fractional cover in Africa. Remote Sens. Environ. 124, 653–665.

Guglielmetti, M., Schwank, M., Mätzler, C., Oberdörster, C., Vanderborght, J., Flühler, H., 2007. Measured microwave radiative transfer properties of a deciduous forest canopy. Remote Sens. Environ. 109, 523–532.

Holmes, T., De Jeu, R., Owe, M., Dolman, A., 2009. Land surface temperature from Ka band (37 GHz) passive microwave observations. J. Geophys. Res. Atmos. 114.

Hornbuckle, B., Walker, V., Eichinger, B., Wallace, V., Yildirim, E., 2017. Soil surface roughness observed during SMAPVEX16-IA and its potential consequences for SMOS and SMAP. In: 2017 IEEE International Geoscience and Remote Sensing Symposium (IGARSS). IEEE, pp. 2027–2030.

Hovmöller, E., 1949. The trough-and-ridge diagram. Tellus 1, 62–66.

Huete, A., Didan, K., Miura, T., Rodriguez, E.P., Gao, X., Ferreira, L.G., 2002. Overview of the radiometric and biophysical performance of the MODIS vegetation indices. Remote Sens. Environ. 83, 195–213.

Imaoka, K., Maeda, T., Kachi, M., Kasahara, M., Ito, N., Nakagawa, K., 2012. Status of AMSR2 instrument on GCOM-W1. In: Earth Observing Missions and Sensors: Development, Implementation, and Characterization II. International Society for Optics and Photonics, p. 852815.

Jackson, T.J., 1993. III. Measuring surface soil moisture using passive microwave remote sensing. Hydrol. Process. 7, 139–152.

Jackson, T., Schmugge, T., 1991. Vegetation effects on the microwave emission of soils. Remote Sens. Environ. 36, 203–212.

Jackson, T.J., Chen, D., Cosh, M., Li, F., Anderson, M., Walthall, C., Doriaswamy, P., Hunt, E.R., 2004. Vegetation water content mapping using Landsat data derived normalized difference water index for corn and soybeans. Remote Sens. Environ. 92, 475–482.

Jones, L.A., Ferguson, C.R., Kimball, J.S., Zhang, K., Chan, S.T.K., McDonald, K.C., Njoku, E.G., Wood, E.F., 2010. Satellite microwave remote sensing of daily land surface air temperature minima and maxima from AMSR-E. IEEE J. Select. Topics Appl. Earth Observ. Remote Sens. 3, 111–123.

Jones, M.O., Jones, L.A., Kimball, J.S., McDonald, K.C., 2011. Satellite passive microwave remote sensing for monitoring global land surface phenology. Remote Sens. Environ. 115, 1102–1114.

Jones, M.O., Kimball, J.S., Jones, L.A., 2013. Satellite microwave detection of boreal forest recovery from the extreme 2004 wildfires in Alaska and Canada. Glob. Chang. Biol. 19, 3111–3122.

Jones, M.O., Kimball, J.S., Nemani, R.R., 2014. Asynchronous Amazon forest canopy phenology indicates adaptation to both water and light availability. Environ. Res. Lett. 9.

Karthikeyan, L., Pan, M., Konings, A.G., Piles, M., Fernandez-Moran, R., Nagesh Kumar, D., Wood, E.F., 2019. Simultaneous retrieval of global scale vegetation optical depth, surface roughness, and soil moisture using X-band AMSR-E observations. Remote Sens. Environ. 234, 111473.

Kerr, Y.H., Waldteufel, P., Wigneron, J.-P., Delwart, S., Cabot, F., Boutin, J., Escorihuela, M.-J., Font, J., Reul, N., Gruhier, C., 2010. The SMOS mission: new tool for monitoring key elements of the global water cycle. Proc. IEEE 98, 666–687.

Koike, T., Nakamura, Y., Kaihotsu, I., Davaa, G., Matsuura, N., Tamagawa, K., Fujii, H., 2004. Development of an advanced microwave scanning radiometer (AMSR-E) algorithm for soil moisture and vegetation water content. Proc. Hydraul. Eng. 48, 217–222.

Konings, A.G., Gentine, P., 2017. Global variations in ecosystem-scale isohydricity. Glob. Chang. Biol. 23, 891–905.

Konings, A.G., Piles, M., Rötzer, K., McColl, K.A., Chan, S.K., Entekhabi, D., 2016. Vegetation optical depth and scattering albedo retrieval using time series of dual-polarized L-band radiometer observations. Remote Sens. Environ. 172, 178–189.

Konings, A.G., Piles, M., Das, N., Entekhabi, D., 2017. L-band vegetation optical depth and effective scattering albedo estimation from SMAP. Remote Sens. Environ. 198, 460–470.

Konings, A.G., Rao, K., Steele-Dunne, S.C., 2019. Macro to micro: microwave remote sensing of plant water content for physiology and ecology. New Phytol. 223, 1166–1172.

Lawrence, H., Wigneron, J.-P., Richaume, P., Novello, N., Grant, J., Mialon, A., Al Bitar, A., Merlin, O., Guyon, D., Leroux, D., Bircher, S., Kerr, Y., 2014. Comparison between SMOS vegetation optical depth products and MODIS vegetation indices over crop zones of the USA. Remote Sens. Environ. 140, 396–406.

Li, X., Al-Yaari, A., Schwank, M., Fan, L., Frappart, F., Swenson, J., Wigneron, J.P., 2020a. Compared performances of SMOS-IC soil moisture and vegetation optical depth retrievals based on tau-omega and two-stream microwave emission models. Remote Sens. Environ. 236, 111502.

Li, X., Wigneron, J.P., Frappart, F., Fan, L., Wang, M., Liu, X., Al-Yaari, A., Moisy, M., 2020b. Development and validation of the SMOS-IC version 2 (V2) soil moisture product. In: IGARSS 2020–2020 IEEE International Geoscience and Remote Sensing Symposium. IEEE.

Liu, Y., de Jeu, R.A.M., van Dijk, A.I.J.M., Owe, M., 2007. TRMM-TMI satellite observed soil moisture and vegetation density (1998–2005) show strong connection with El Niño in eastern Australia. Geophys. Res. Lett. 34.

Liu, Y.Y., de Jeu, R.A.M., McCabe, M.F., Evans, J.P., van Dijk, A.I.J.M., 2011. Global long-term passive microwave satellite-based retrievals of vegetation optical depth. Geophys. Res. Lett. 38.

Liu, Y.Y., van Dijk, A.I.J.M., de Jeu, R.A.M., Canadell, J.G., McCabe, M.F., Evans, J.P., Wang, G., 2015. Recent reversal in loss of global terrestrial biomass. Nat. Clim. Chang. 5, 470–474.

Liu, Y.Y., van Dijk, A.I.J.M., Miralles, D.G., McCabe, M.F., Evans, J.P., de Jeu, R.A.M., Gentine, P., Huete, A., Parinussa, R.M., Wang, L., Guan, K., Berry, J., Restrepo-Coupe, N., 2018. Enhanced canopy growth precedes senescence in 2005 and 2010 Amazonian droughts. Remote Sens. Environ. 211, 26–37.

Liu, X., Wigneron, J.P., Frappart, F., Baghdadi, N., Zribi, M., Jagdhuber, T., Li, X., Wang, M., Fan, L., Moisy, M., 2020. New ASCAT vegetation optical depth (IB-VOD) retrievals over Africa. In: IGARSS 2020–2020 IEEE International Geoscience and Remote Sensing Symposium. IEEE.

Ma, H., Zeng, J., Chen, N., Zhang, X., Cosh, M.H., Wang, W., 2019. Satellite surface soil moisture from SMAP, SMOS, AMSR2 and ESA CCI: a comprehensive assessment using global ground-based observations. Remote Sens. Environ. 231, 111215.

Meesters, A.G., De Jeu, R.A., Owe, M., 2005. Analytical derivation of the vegetation optical depth from the microwave polarization difference index. IEEE Geosci. Remote Sens. Lett. 2, 121–123.

Mironov, V.L., Dobson, M.C., Kaupp, V.H., Komarov, S.A., Kleshchenko, V.N., 2004. Generalized refractive mixing dielectric model for moist soils. IEEE Trans. Geosci. Remote Sens. 42, 773–785.

Mironov, V.L., Kosolapova, L.G., Fomin, S.V., Savin, I.V., 2019. Experimental analysis and empirical model of the complex permittivity of five organic soils at 1.4 GHz in the temperature range from −30 °C to 25 °C. IEEE Trans. Geosci. Remote Sens. 57, 3778–3787.

Mladenova, I.E., Jackson, T.J., Njoku, E., Bindlish, R., Chan, S., Cosh, M.H., Holmes, T.R. H., de Jeu, R.A.M., Jones, L., Kimball, J., Paloscia, S., Santi, E., 2014. Remote monitoring of soil moisture using passive microwave-based techniques — Theoretical basis and overview of selected algorithms for AMSR-E. Remote Sens. Environ. 144, 197–213.

Mo, T., Choudhury, B.J., Schmugge, T.J., Wang, J.R., Jackson, T.J., 1982. A model for microwave emission from vegetation-covered fields. J. Geophys. Res. 87.

Moesinger, L., Dorigo, W., de Jeu, R., van der Schalie, R., Scanlon, T., Teubner, I., Forkel, M., 2020. The global long term microwave vegetation optical depth climate archive (VODCA). Earth Syst. Sci. Data 12, 177–196.

Montpetit, B., Royer, A., Wigneron, J.P., Chanzy, A., Mialon, A., 2015. Evaluation of multi-frequency bare soil microwave reflectivity models. Remote Sens. Environ. 162, 186–195.

Njoku, E.G., Jackson, T.J., Lakshmi, V., Chan, T.K., Nghiem, S.V., 2003. Soil moisture retrieval from AMSR-E. IEEE Trans. Geosci. Remote Sensi. 41, 215–229.

O'Neill, P., Njoku, E., Jackson, T., Chan, S., Bindlish, R., 2015. SMAP Algorithm Theoretical Basis Document: Level 2 & 3 Soil Moisture (Passive) Data Products. Jet Propulsion Lab., California Inst. Technol. Pasadena, CA, USA, JPL D-66480.

Owe, M., de Jeu, R., Holmes, T., 2008. Multisensor historical climatology of satellite-derived global land surface moisture. J. Geophys. Res. Earth Surf. 113.

Parrens, M., Wigneron, J.-P., Richaume, P., Mialon, A., Al Bitar, A., Fernandez-Moran, R., Al-Yaari, A., Kerr, Y.H., 2016. Global-scale surface roughness effects at L-band as estimated from SMOS observations. Remote Sens. Environ. 181, 122–136.

Patton, J., Hornbuckle, B., 2012. Initial validation of SMOS vegetation optical thickness in Iowa. IEEE Geosci. Remote Sens. Lett. 10, 647–651.

Rodríguez-Fernández, N.J., Mialon, A., Mermoz, S., Bouvet, A., Richaume, P., Al Bitar, A., Al-Yaari, A., Brandt, M., Kaminski, T., Le Toan, T., Kerr, Y.H., Wigneron, J.-P., 2018. An evaluation of SMOS L-band vegetation optical depth (L-VOD) data sets: high sensitivity of L-VOD to above-ground biomass in Africa. Biogeosciences 15, 4627–4645.

Saatchi, S.S., Harris, N.L., Brown, S., Lefsky, M., Mitchard, E.T., Salas, W., Zutta, B.R., Buermann, W., Lewis, S.L., Hagen, S., 2011. Benchmark map of forest carbon stocks in tropical regions across three continents. Proc. Natl. Acad. Sci. 108, 9899–9904.

Sadeghi, M., Ebtehaj, A., Crow, W.T., Gao, L., Purdy, A.J., Fisher, J.B., Jones, S.B., Babaeian, E., Tuller, M., 2020. Global estimates of land surface water fluxes from SMOS and SMAP satellite soil moisture data. J. Hydrometeorol. 21, 241–253.

Saleh, K., Wigneron, J.-P., De Rosnay, P., Calvet, J.-C., Escorihuela, M.J., Kerr, Y., Waldteufel, P., 2006. Impact of rain interception by vegetation and mulch on the L-band emission of natural grass. Remote Sens. Environ. 101, 127–139.

Saleh, K., Wigneron, J.-P., Waldteufel, P., De Rosnay, P., Schwank, M., Calvet, J.-C., Kerr, Y., 2007. Estimates of surface soil moisture under grass covers using L-band radiometry. Remote Sens. Environ. 109, 42–53.

Scanlon, T., Pasik, A., Dorigo, W., De Jeu, R., Hahn, S., Van der Schalie, R., Wagner, W., Kidd, R., Gruber, A., Moesinger, L., Preimesberger, W., 2020. Algorithm Theoretical Baseline Document (ATBD) D2. 1 Version 04.7. Available at. https://www.esa-soilmoisture-cci.org/sites/default/files/documents/public/CCI%20SM%20v04.7%20documentation/ESA_CCI_Soil_Moisture_Algorithm_Theoretical_Basis_Document_(ATBD)_v04.7.pdf. Access Date: 12 March 2020. In. ESA Climate Change Initiative Plus - Soil Moisture.

Simard, M., Pinto, N., Fisher, J.B., Baccini, A., 2011. Mapping forest canopy height globally with spaceborne lidar. J. Geophys. Res. Biogeosci. 116.

Simpson, E.H., 1949. Measurement of diversity. Nature 163, 688.

Teubner, I.E., Forkel, M., Camps-Valls, G., Jung, M., Miralles, D.G., Tramontana, G., van der Schalie, R., Vreugdenhil, M., Mösinger, L., Dorigo, W.A., 2019. A carbon sink-driven approach to estimate gross primary production from microwave satellite observations. Remote Sens. Environ. 229, 100–113.

Tian, F., Brandt, M., Liu, Y.Y., Verger, A., Tagesson, T., Diouf, A.A., Rasmussen, K., Mbow, C., Wang, Y., Fensholt, R., 2016. Remote sensing of vegetation dynamics in drylands: evaluating vegetation optical depth (VOD) using AVHRR NDVI and in situ green biomass data over West African Sahel. Remote Sens. Environ. 177, 265–276.

Tian, F., Wigneron, J.-P., Ciais, P., Chave, J., Ogee, J., Penuelas, J., Raebild, A., Domec, J. C., Tong, X., Brandt, M., Mialon, A., Rodriguez-Fernandez, N., Tagesson, T., Al-Yaari, A., Kerr, Y., Chen, C., Myneni, R.B., Zhang, W., Ardo, J., Fensholt, R., 2018. Coupling of ecosystem-scale plant water storage and leaf phenology observed by satellite. Nat. Ecol. Evol. 2, 1428–1435.

Togliatti, K., Hartman, T., Walker, V.A., Arkebauer, T.J., Suyker, A.E., VanLoocke, A., Hornbuckle, B.K., 2019. Satellite L-band vegetation optical depth is directly proportional to crop water in the us corn belt. Remote Sens. Environ. 233, 111378.

Tong, X., Tian, F., Brandt, M., Liu, Y., Zhang, W., Fensholt, R.J.R.S.o.E., 2019. Trends of land surface phenology derived from passive microwave and optical remote sensing systems and associated drivers across the dry tropics 1992–2012. Remote Sens. Environ. 232, 111307.

van der Schalie, R., de Jeu, R.A.M., Kerr, Y.H., Wigneron, J.P., Rodríguez-Fernández, N. J., Al-Yaari, A., Parinussa, R.M., Mecklenburg, S., Drusch, M., 2017. The merging of radiative transfer based surface soil moisture data from SMOS and AMSR-E. Remote Sens. Environ. 189, 180–193.

Vrije Universiteit Amsterdam (Richard de Jeu) and NASA GSFC (Manfred Owe), 2014. AMSR2/GCOM-W1 surface soil moisture (LPRM) L3 1 day 25 km x 25 km ascending V001. Goddard Earth Sciences Data and Information Services Center (GES DISC) (Bill Teng), Greenbelt, MD, USA, Goddard Earth Sciences Data and Information Services Center (GES DISC). https://doi.org/10.5067/M5DTR2QUYLS2. Accessed: [1 March 2020].

Wang, J., Choudhury, B., 1981. Remote sensing of soil moisture content, over bare field at 1.4 GHz frequency. J. Geophys. Res. Oceans 86, 5277–5282.

Wang, J.R., Schmugge, T.J., 1980. An empirical model for the complex dielectric permittivity of soils as a function of water content. IEEE Trans. Geosci. Remote Sens. 288–295.

Weber, M., Hao, D., Asrar, G.R., Zhou, Y., Li, X., Chen, M., 2020. Exploring the use of DSCOVR/EPIC satellite observations to monitor vegetation phenology. Remote Sens. 12, 2384.

Wigneron, J.-P., Waldteufel, P., Chanzy, A., Calvet, J.-C., Kerr, Y., 2000. Two-dimensional microwave interferometer retrieval capabilities over land surfaces (SMOS mission). Remote Sens. Environ. 73, 270–282.

Wigneron, J.P., Kerr, Y., Waldteufel, P., Saleh, K., Escorihuela, M.J., Richaume, P., Ferrazzoli, P., de Rosnay, P., Gurney, R., Calvet, J.C., Grant, J.P., Guglielmetti, M., Hornbuckle, B., Mätzler, C., Pellarin, T., Schwank, M., 2007. L-band microwave emission of the biosphere (L-MEB) model: description and calibration against experimental data sets over crop fields. Remote Sens. Environ. 107, 639–655.

Wigneron, J.P., Jackson, T.J., O'Neill, P., De Lannoy, G., de Rosnay, P., Walker, J.P., Ferrazzoli, P., Mironov, V., Bircher, S., Grant, J.P., Kurum, M., Schwank, M., Munoz-Sabater, J., Das, N., Royer, A., Al-Yaari, A., Al Bitar, A., Fernandez-Moran, R., Lawrence, H., Mialon, A., Parrens, M., Richaume, P., Delwart, S., Kerr, Y., 2017. Modelling the passive microwave signature from land surfaces: a review of recent results and application to the L-band SMOS & SMAP soil moisture retrieval algorithms. Remote Sens. Environ. 192, 238–262.

Wigneron, J.P., Li, X., Frappart, F., Fan, L., Al-Yaari, A., De Lannoy, G., Liu, X., Wang, M., Le Masson, E., & Moisy, M. n.d..SMOS-IC data record of soil moisture and L-VOD: historical development, applications and perspectives. Remote Sens. Environ. Submitted for publication.

Wigneron, J.-P., Mialon, A., De Lannoy, G., Fernandez-Moran, R., Al-Yaari, A., Ebrahimi, M., Rodriguez-Fernandez, N., Kerr, Y., Quets, J., Pellarin, T., 2018. SMOS-IC: Current status and overview of soil moisture and VOD applications. In: IGARSS 2018–2018 IEEE International Geoscience and Remote Sensing Symposium. IEEE, pp. 1451–1453.

Wigneron, J.-P., Fan, L., Ciais, P., Bastos, A., Brandt, M., Chave, J., Saatchi, S., Baccini, A., Fensholt, R., 2020. Tropical forests did not recover from the strong 2015–2016 El Niño event. Sci. Adv. 6, eaay4603.